Characterising interfaces for reinforced concrete: experiments and multiplane cohesive zone modelling for Titanium alloy rebars

Diletta Maracci[a*], Giulio Alfano[b], Roberto Serpieri[c], Stefano Lenci[a]

(a) Dipartimento di Ingegneria Civile, Edile e Architettura, Università Politecnica delle Marche, Via Brecce Bianche, 12 - 60131 Ancona, Italy

(b) School of Engineering and Design, Brunel University, Kingston Lane, UB8 3PH Uxbridge, UK

(c) Dipartimento di Ingegneria, Università degli Studi del Sannio, Piazza Roma, 21 - I, 82100 Benevento, Italy

[*]Corresponding author: d.maracci@pm.univpm.it

Abstract

This paper addresses the experimental and numerical characterisation of the structural interface between titanium alloy Ti6Al4V plain bars and Normal (NWC) and Light-Weight Concrete (LWC) mixtures. Results of pull-out tests on $\phi 8$ and $\phi 16$ mm rebars from NWC and LWC batches and SEM analyses show that, although the employed rebars are plain, the debonding process is strongly affected by defects-induced surface roughness still present at the microscopic level, which activates mechanical interlocking responsible for the dilatant behaviour of the interface.

Experimental tests are supported by Finite Element (FE) analyses employing Cohesive Zone Models (CZMs) for simulating the interfacial delamination. To this end, the micromechanics-based CZM proposed by Serpieri et al., accounting for damage, friction and interlocking, is employed, upon extending this formulation by addressing the degradation of the depth of asperities as a novel mechanical feature, Sensitivity analyses permit to assess the proposed modelling strategy and to devise a procedure for the numerical identification of model parameters. Experimental pull-out curves are fitted by employing a single set of material parameters for each concrete batch, achieving reasonable numerical-experimental agreement for tests with both $\phi 8$ and $\phi 16$ mm, thus showing good predictivity of the proposed modelling strategy.

Keywords: titanium-concrete interface; pull-out test; cohesive zone models.

1 Introduction

Over decades many efforts have been made by researchers to improve the durability of Reinforced Concrete (RC) structures, such as adding corrosion inhibitors in the concrete mixture [1] and coating the steel rebar surface with both metallic (galvanized steel [2]) and organic (epoxy-coated steel [3]) films so as to improve reinforcements corrosion resistance. In addition, the possibility to reinforce concrete with alternative materials less susceptible to corrosion than carbon steel has been often explored. Among metallic reinforcements, some studies have investigated the behaviour of nickel-iron alloys [4] and, particularly, stainless steel reinforcing bars [5] [6]. A lot of research has been also focused on non-metallic materials, especially concerning Fibre Reinforced Polymers (FRP) [7], such as the better known Carbon (CFRP), Glass (GFRP) and Aramid (AFRP) Fibre Reinforced Polymers [8], and the recently proposed Basalt Fibre Reinforced Plastic (BFRP) [9]. Corrosion of embedded reinforcements on structural capacity not only concerns the reinforcement itself and the surrounding concrete, but also changes the interaction between the two. In fact, the reduction of bar cross-section and increase in bar diameter resulting from the volumetric expansion of corrosion products, strongly

affect the mechanical characteristics of the bar-matrix interface [10]. Thus, corrosion can significantly reduce the stress transfer mechanism, which is essential to consider RC as a composite structural material [11].

The rebar-matrix interface, however, represents a very complex zone, as recently remarked by Angst et al. [12] in the case of steel reinforcement. This zone, indeed, exhibits significant spatial heterogeneity of physical and chemical properties due to the possible presence of meso-structured and/or micro-structured geometry (in short *asperities*) in the bar itself and/or in the surrounding concrete material, and also due to the occurrence of defects such as voids, honeycombs, cracks, and bleed water zones. A proper description of asperities and of defects, by a more phenomenological rationale or micro-mechanical rationale, consequently appears to be essential in both experimental and theoretical research. For all these reasons, a prerequisite for the application of alternative reinforcements is the understanding of the interfacial behaviour between them and concrete, i.e. the bond performance. In fact, establishing the interface bond properties under the simplest possible geometrical conditions seems to be a primary necessity whenever new materials for reinforcement (e.g. stainless steel [5] [6], FRP [13], [14], [15]) or novel coatings of steel bars [16], [17] are investigated.

Concerning the experimental investigation of the performances of reinforcement-concrete bond, a primary method for understanding the underlying failure mechanisms is represented by *pull-out tests* [18] which provide the so-called *bond-slip* relationships. Data from a large amount of pull-out tests are currently available for different types of concrete matrices (such as high-strength [19], fibre reinforced [20], recycled aggregate [21], lightweight aggregate [22]) as well as of different types of reinforcing materials (e.g., bars made of steel [18], FRPs [13], [14], [15], aluminium [23], epoxy-coated steel [16]), and bar geometries [24]. It is well known, for instance, that ribbed or deformed bars subjected to pull-out tests from a concrete matrix may lead to the so-called *splitting failure* [18]. In this failure mechanism the bond resistance is mainly provided by an interlocking effect between rebar lugs and concrete, originating the cracking formation process of the matrix surrounding the rebar. Conversely, plain rebars, always fail due to a pure *pull-out* mechanism, characterised by the loss of the two main contributions to bond: chemical adhesion and friction [17], [25], [26]. In plain bars, although bond strength values are much lower than those observed for deformed bars, the bond characteristics can be considered more representative of the actual interaction at the material interface between matrix and reinforcements since the typical failure mechanism is not constrained by the splitting phenomenon [25]. For plain rebars, the effect on the bond behaviour of surface treatments, such as sandblast of steel bars [25] or sand-coating of FRP ones [13], has been also investigated in the literature. Experimental evidence shows that surface treatments usually increase the reinforcement surface roughness, resulting in higher bond strengths under pull-out conditions. Despite the proven influence of the rebar surface roughness on bond capacity, its role on the interfacial mechanisms during the pull-out failure seems, however, to need further investigation [25].

Pull-out test results can be seen as the macroscopic response of the rebar-matrix debonding process occurring at a lower scale. To better evaluate the interfacial micro-mechanisms having a role in that process, Finite Element (FE) analysis can be employed, as long as the numerical model incorporates sufficient aspects of such micromechanics. Cohesive-zone models (CZMs) have become a popular numerical tool for modelling fracture in solids in FE-based analyses [27]. After the pioneering papers by Dugdale [28], Barenblatt [29] and Hilleborg et al. [30], a considerably large family of CZMs has been proposed in the literature because of the variety of mechanical and numerical issues involved and of the broad range of possible applications (see [27] and [31] for a detailed review). A first straight classification can be made upon the shape of the cohesive law,

i.e. the normal (or tangential) traction vs. the normal (or tangential) separation. The four shapes more frequently employed for the cohesive law are [32]: bilinear (e.g. Hilleborg et al. [30], Alfano and Crisfield [33]), linear-parabolic (e.g. Allix and Corigliano [34]), exponential (e.g. Xu and Needleman [35], Chandra et al. [36]) and trapezoidal (e.g. Tvergaard and Hutchinson [37]). For all these CZMs the traction-separation laws are such that by increasing interfacial separation, the traction across the interface reaches a maximum, then decreases and eventually vanishes till complete decohesion. However, for many engineering applications, and especially for cementitious materials, a crucial aspect is represented by the interplay between the debonding process and friction. CMZs accounting for friction were proposed by Chaboche et al. [38], Lin et al. [39], Del Piero and Raous [40], and Alfano and Sacco [41]. Chaboche et al. take into consideration the friction term since the very beginning of the interfacial law, i.e. before complete decohesion. Lin et al., instead, add the condition that the tangential stress must be lower than the modulus of the normal stress multiplied by the friction coefficient. Several other models, including the one proposed by Del Piero and Raous [40], are based on nonassociative softening plasticity (such as the multidissipative interface model proposed by Cocchetti et al. [42]). A key idea exploited by Alfano and Sacco [41], instead, consists of introducing a unilateral Coulomb friction law on the only damaged part of a so-called Representative Element Area (REA) of the interface. Next, a simplified micromechanical formulation is considered based on an additive decomposition of the REA into an undamaged and a completely damaged part. On the former a linear elastic behaviour is assumed, while on the latter unilateral contact and a Coulomb-type friction law are employed. Damage is assumed to evolve according to a mixed-mode law widely used for debonding and composite delamination. With no softening plasticity, this model has laid the basis for further developments, based on the concept of Representative Interface Area (RIA), able to account for the interlocking effect while preserving thermodynamic consistency, to (see Serpieri and Alfano [43] and Serpieri et al. [44]) and also for finite dilation and asperity degradation (model developed by Serpieri, Alfano and Sacco [45]). In the first model the interlocking phenomenon is simulated assuming the presence at the microscale level (i.e. at the integration point) of a periodic pattern of distinct inclined elementary planes (or *microplanes*) simulating interface asperities, and has been for this reason recently denominated Multiplane-CZM (M-CZM) [46]. Each elementary plane is, in its turn, governed by the combined cohesive-friction model by Alfano and Sacco [41]. The enhanced features introduced in [45] permit to account for the finite depth of the asperities by considering the progressive reduction in contact area between each couple of interfacing microplanes for increasing opening (macro-scale) relative displacement. A progressive reduction of the microplanes inclination angles is then able to capture asperities rupture and associated flattening of the fracture surface. This model is referred to in short as '*angle-degrading* M-CZM'.

The present work concerns the characterisation of the interfacial behaviour between the titanium alloy Ti6Al4V, also known as 'Grade 5' [47], and concrete. Titanium is a material that has never been thoroughly investigated as potential reinforcement of concrete structures, clearly because of its cost. To the best of the authors' knowledge, only few studies [4], [48] have mentioned the possibility to use titanium alloy bars in RC structures as corrosion protection method. Recently, however, Higgins et al. [49] proposed a novel application of titanium alloy bars for the flexural and shear strengthening of RC beams. Thus, for special designs where avoiding rebar corrosion and reducing structure self-weight are crucial to the point to justify high expenses, titanium, with its outstanding corrosion resistance [50], may become a realistic option. Nevertheless, there still is lack of information about the bond relationship that titanium and concrete can develop, which, however, represents a crucial step towards the possibility to combine them in a composite structural material. To fill this

gap, a series of pull-out tests on Ti6Al4V plain bars has been carried out from two different concrete mixtures, differing for the coarse aggregate phase, i.e. normal and light-weight aggregates. Plain bars were selected in order to better understand the influence that the particular material used for the reinforcement and the different types of concrete batches designed have on the pull-out response. Additionally, by using plain rebars and analysing the problem from a micro-mechanical point of view, the role of defects-induced and fracture-induced surface roughness can be more easily identified.

To analyse roughness, the experimental tests have been supplemented by FE analyses in which the angle-degrading M-CZM proposed by Serpieri, Alfano and Sacco [45] is used and then extended introducing, as a novel mechanical feature, the reduction of depth of asperities induced by wear and degradation. The further degradation mechanism allows us to more accurately simulate the residual horizontal plateau exhibited by the experimental bond-slip relationships, which could not be captured by the simpler M-CZM [45] (see Fig. 21 at page 25). The resulting model, denominated '*enhanced degrading M-CZM*', permits to outline the individual role of each damaging mechanism in the overall system response, considering also effects induced by the rebar surface roughness which are usually neglected in the FE simulation of pull-out tests.

The outline of the paper is as follows: Section 2 describes the setup of the pull-out tests carried out and presents test results, including a comprehensive analysis of the literature on bond strength values of materials typically used as reinforcement in RC structures. In Section 3, the experimental results are reproduced through FE models by employing the enhanced-degrading M-CZM. Conclusions are drawn in Section 4.

2 Experimental Testing

2.1 Material properties

Eight Ti6Al4V plain bars of two different diameters, namely 8 and 16 mm, were used in this study. Their tensile strength has been preliminary tested according to the European standard BS EN ISO 6892-1:2009 [51]. Table 1 reports the tensile strength test results and the specifications provided by the manufacturer (TiFast S.r.l.) of the used bars.

Table 1- Mechanical properties of Ti6Al4V bars

Specifications provided by the manufacturer (TiFast S.r.l.)								Tensile Test Results	
Bar diameter	Alloy	Surface finish	Surface roughness	Tensile strength	Yield Strength 0.2% offset	Reduction of area at failure	Elongation	Tensile strength (average)	Elastic Modulus (average)
(mm)			(μm)	(MPa)	(MPa)	(%)	(%)	(MPa)	(GPa)
8	Ti6Al4V	Peeled, Polished	<1.6	957	878	37	16	962.64	110
16	Ti6Al4V	Peeled, Polished	<1.6	980	923	52.3	16.3	961.45	90

Concerning concrete, two different mixtures were cast, i.e. normal (Normal-Weight Concrete, NWC) and lightweight aggregate concrete (Light-Weight Concrete, LWC). In particular, fine aggregate (maximum diameter, D_{max}=4 mm) consists of natural sand for both the mixtures, while coarse one (D_{max}=15 mm) consists of crushed gravel for NWC and expanded clay for LWC mixture. Details of the mix design for both the mixtures are reported in Table 2. The concrete compressive strength was determined through compressive tests on two control samples (100×100 mm cubic specimens) for each batch. The mean concrete strength values, f_{cm}, are presented in the forthcoming Table 3.

Table 2 - NWC and LWC concrete mixtures mix design

NWC mix		(kg/m³)	LWC mix		(kg/m³)
Water		184	Water		184
Cement CEM II A/L 42.5R		335	Cement CEM II A/L 42.5R		420
Fine aggregate (natural sand)	(0-4 mm)	1010	Fine aggregate (natural sand)	(0-4 mm)	785
Coarse aggregate (crushed gravel)	(4-15 mm)	790	Coarse aggregate (Expanded Clay)	(0-15 mm)	340
Superplasticiser		2.7	Superplasticiser		3.4
			Air entraining admixture		2.6
Density		2325	Density		1735

2.2 Specimen preparation and testing setup

The pull-out tests were performed according to RILEM RC 6 standard [52]. A 150 mm cubic mould was used to manufacture the pull-out specimens. According to RILEM RC6 [52], the bond length, l_b, of the bars was made equal to five times the bar diameter, d_s, by using a plastic sleeve and the bars were placed so that they extend beyond the two sides of the specimens (see Fig. 1a). Particularly, the free end length was equal to 300 mm, as specified by RILEM RC6 [52]. The concrete was cast with the Ti6Al4V bars in horizontal position inside the mould, in the middle of the specimen, by placing a support under the bar portion exceeding the mould. After moulding, the specimens were transferred to a curing room for 24 h at a temperature of 20 ± 2 °C and a relative humidity of $60 \pm 5\%$. Thereafter, the concrete cubes were de-moulded and stored again under the same temperature and humidity conditions.

The pull-out test setup is shown in Fig. 1b. A total of eight specimens with the same characteristics two by two, were tested. Tests were performed with the displacement control setting to track the post-peak behaviour. The loading rate has been set equal to 0.05 mm/s and the recording data frequency was 10 Hz. In order to better evaluate the properties of the Ti6Al4V-concrete interface, for one of each pair of specimens, the bar was not completely pulled out from the matrix and then the specimen was cut transversally. The cut position was chosen to capture both the matrix and the part of the bar not fully pulled out. Therefore, the cross-section obtained through this process could be observed with the Scanning Electron Microscope (SEM).
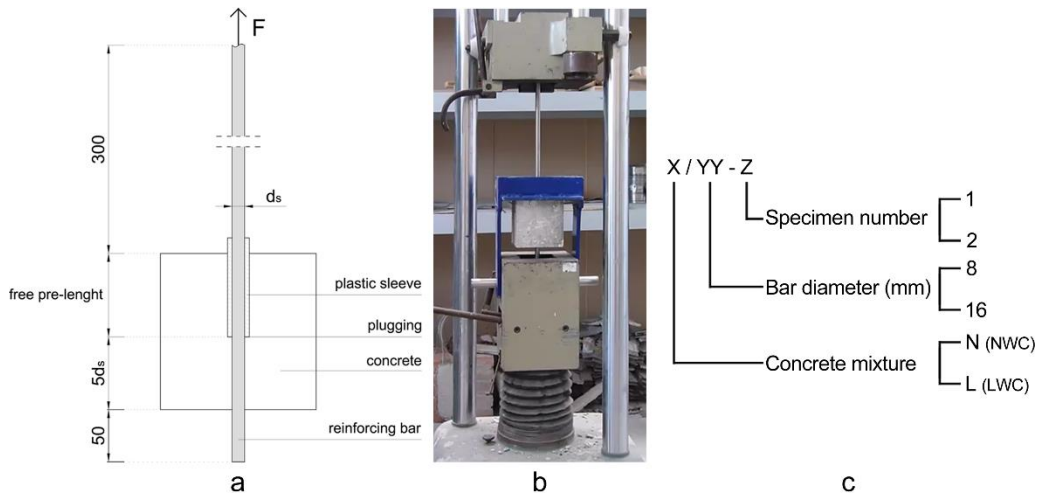

Fig. 1 - a) pull-out test scheme; b) pull-out test setup; c) specimen identification for the pull-out test

2.3 Test results and discussion

The tensile force, F, measured in the test is transformed into bond stress, τ_{dm}, by Eq. (1).

$$\tau_{dm} = \frac{F}{\pi d_s l_b} \tag{1}$$

5

The bond strength, τ_{max}, is the maximum value reached by τ_{dm}, i.e. the one obtained inserting in Eq. (1) the peak force F_{max} of the bond stress-slip relationship. Fig. 1c shows the notation used to identify the pull-out specimens, while the experimental results obtained from the tests are summarised in Table 3, where f_{cm} is the mean value of the compressive strength for each concrete batch and the slip value of the loaded end at bond strength is indicated as s_{bs}. A normalised bond strength, τ_{dm}^* ([25] and [14]), with respect to the square root of concrete compressive strength has been also computed through Eq. (2) in order to make a comparison between the obtained results among the two types of concrete mixture.

$$\tau_{dm}^* = \frac{\tau_{dm}}{\sqrt{f_{cm}}}$$ (2)

Table 3 - Experimental pull-out test results

Specimen	f_{cm} (MPa)	F_{max} (kN)	$\tau_{dm,max}$ (MPa)	s_{bs} (mm)	$\tau *_{dm,max}$ (MPa$^{0.5}$)	Fully/Partially pulled-out (F / P)
N/8-1	42	2.00	1.99	0.601	0.31	F
N/8-2 **	42	-	-	-	-	-
N/16-1	42	6.80	1.69	0.937	0.26	F
N/16-2	42	7.50	1.87	0.669	0.29	P
L/8-1	29	2.97	2.95	1.031	0.55	F
L/8-2	29	2.75	2.74	0.857	0.51	P
L/16-1	29	10.75	2.67	1.083	0.50	F
L/16-2	29	10.10	2.51	1.044	0.47	P

** Specimen N/8-2 failed the test for a sliding between the rebar end and the clamp device. Its response cannot be taken into account.

2.3.1 Bond stress-slip relationship

Fig. 2 and Fig. 3 present the obtained bond stress-slip curves, reporting also the displacement threshold adopted to stop the test of those specimens scheduled for cutting. Fig. 2a shows the response curve of specimen N/8-1 and the failure of the N/8-2 due to sliding between the bar and the clamp device of the testing machine.
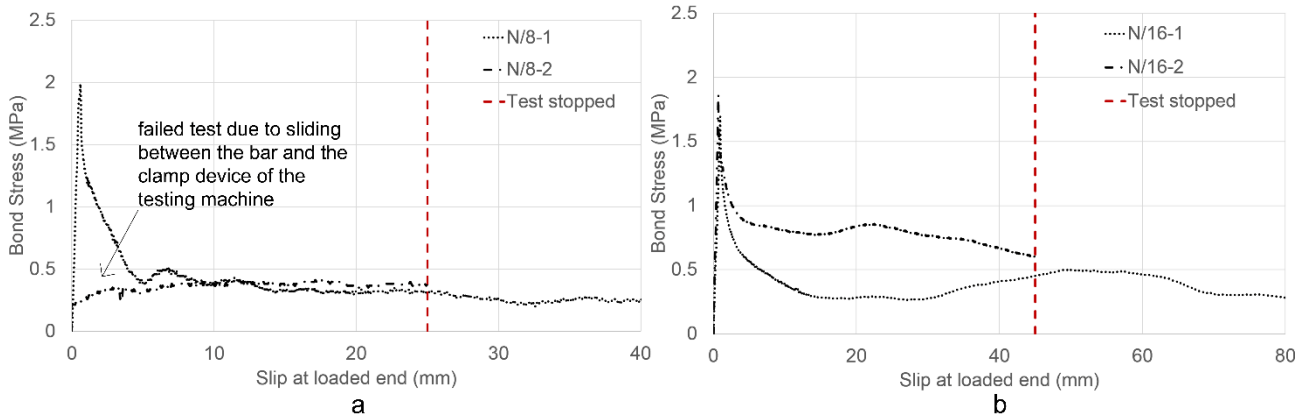

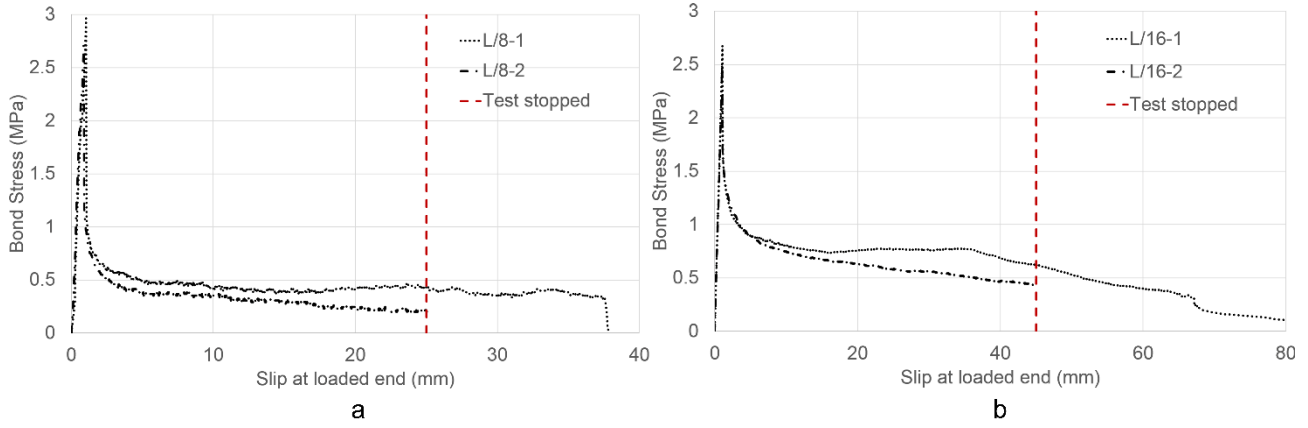Fig. 2 - Pull-out results for NWC: a) ϕ8 mm Ti6Al4V rebars; b) ϕ16 mm Ti6Al4V rebars

Fig. 3 - Pull-out results for LWC: a) ϕ8 mm Ti6Al4V rebars; b) ϕ16 mm Ti6Al4V rebars

Despite few tests were performed, some common features can be extracted from the graphs of Figs. 2 and 3. For both types of concrete, the shear strengths found for the two different diameters is comparable, although the total pull-out force is obviously higher for the φ16 bar shown later in the article. All the bond-slip curves, in fact, exhibit a pull-out failure characterised by an initial almost linear branch up to the pull-out force peak value (corresponding to the bond strength), followed by a sudden decrease in the stress that suggests a significant adhesion reduction. Afterwards, the average bond stress shows a global declining trend without vanishing until the bar is fully pulled-out. The overall decay is gradual, which can be attributed to the presence of friction and the simultaneous progressive reduction of embedded length. Nevertheless, especially the curves obtained in the case of NWC specimens (Figs. 2a and 2b) show some local boosts of the bond stress during the post-peak phase. These local maximums could be explained by conjecturing the presence of a rough fracture surface originated during the pull-out test. It is hypothesised that, even for plain bars, surface roughness can play a significant role in the developing of bond stresses along the interface by originating mechanical interlocking. The latter yields non-negligible effects on bond performance, although it is characterised by a lower geometrical scale and less geometric regularity that that produced by lugs in ribbed bars. In other words, the graphs shown in Figs. 2 and 3 suggest a dilatant behaviour [53] of the rebar-matrix interface, namely its volumetric expansion associated to the shear displacement. To verify this behaviour and to establish the geometric scale of the hypothesised micro-scale interlocking phenomenon, some SEM observations on cut specimens have been carried out. Fig. 4a reports the cut position on the specimens previously tested through the partial pull-out of titanium alloy bars from the concrete matrices. Thus, the obtained cross-section (Fig. 4b) refers to a slip value equal to 55% of the bond length. This value allows for maintaining a segment of the bar portion previously embedded in the concrete matrix within the initial bond zone (Fig. 4a), without losing significant information in the bond-slip relationships. By zooming on the bar-matrix interface (Fig. 4c), the SEM can capture the occurrence of micro-cracks, voids, aggregates, concrete particles (Fig. 5a), showing that the interface represents a very complex area, as noted by Angst et al. [12]. A further zoom on the interface (Fig. 5b) allows for the measurement of the actual separation between the bar and matrix surfaces, whose magnitude is around 10-15 μm on average. Moreover, Fig. 5b reveals the presence of some residual matrix material both attached to the bar surface and in the form of loose particles at the interface. Therefore, these observations seem to confirm the hypothesis above on the dilatant behaviour of the interface. In fact, it has been found that the interface is actually dilated after a slip corresponding to 55% of the bond length. A possible responsible for this phenomenon is represented by a rough interface originated by the

combination of rebar original roughness (1-2 μm) and the presence of concrete particles, both attached to the bar surface and loose at the interface (of the order of 10-20 μm).
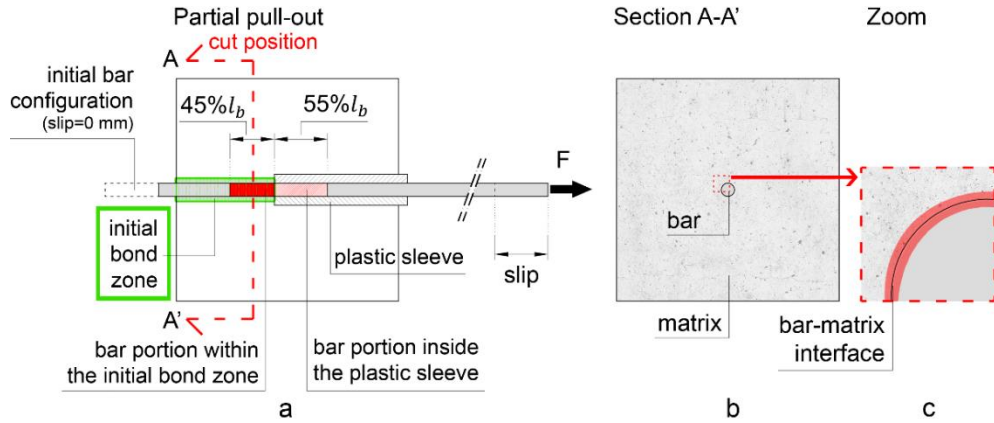

Fig. 4 - a) partial pull-out test and cut position; b) cross-section; c) bar-matrix interface intended for SEM observations
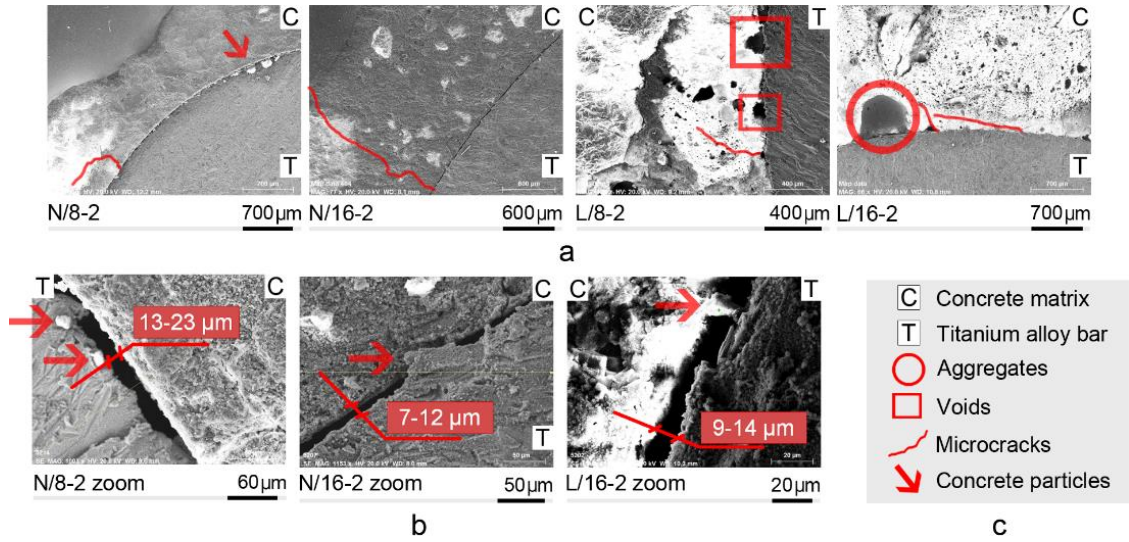

Fig. 5 - SEM observations: a) Bar-matrix interfaces of N/8-2, N/16-2, L/8-2 and L/16-2 specimens with indication of the main features; b) Zoom on the interface of N/8-2, N/16-2 and L/16-2 specimens with the indication of the interface measures; c) Legend

Additional elements corroborating the hypothesis of the presence of an irregular fracture surface are reported in the next paragraph.

2.3.2 Influence of concrete mixture

Two different concrete mixtures, NWC and LWC, have been tested in the present study. Despite the measured compressive strength of LWC is significantly lower (29 MPa) than that of NWC (42 MPa), the mean bond strength value resulted from the tests on LWC is higher than that on NWC specimens. In particular, by comparing the normalised bond strength values, it emerges that the average is 0.51 $MPa^{0.5}$ for LWC while NWC specimens achieve an average value of 0.29 $MPa^{0.5}$. A possible explanation for this peculiar and non-negligible phenomenon could refer to the grain distribution curves of the types of the aggregates used, because the other mixture components are the same and the maximum aggregate diameter is fixed. The other important difference between the two investigated batches consists in the nature of the coarse aggregate phase, i.e. normal-weight crushed gravel and light-weight expanded clay ones, but the developed bond strength does not seem to depend on the chemical bond between rebars and aggregates as much as that between rebars and cement. In fact, as remarked by Angst et al. [12] for the case of steel rebars, the concrete part of the interface

8

zone can be assumed similar to the interfacial transition zone between cement paste and aggregate particles. In other words, it is reasonable to assume that the reinforcement is mostly in contact with the cement phase of the concrete matrix and not with the aggregates. This suggests that other phenomena depending more on the aggregates physical distribution than on their chemical nature, affect the bond-slip behaviour at the interface. By observing the specimen rupture surfaces from the indirect tensile tests of the two studied mixtures (Fig. 6a), it can be noticed that the LWC fracture surface (Fig. 6c) appears more homogeneous than that of NWC (Fig. 6b) in terms of voids, honeycombs and especially of aggregates spatial distribution.
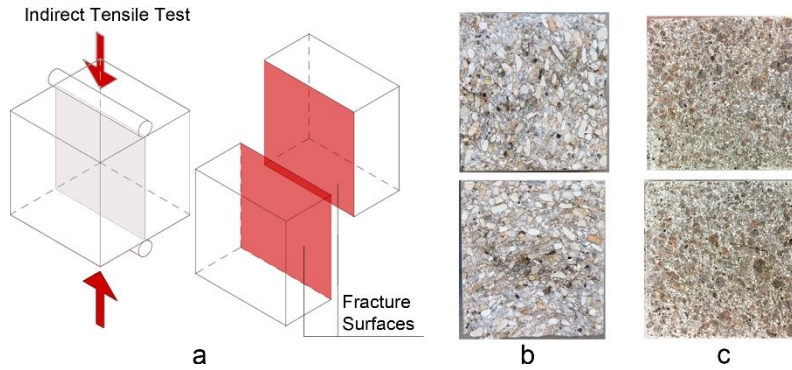

Fig. 6 - Indirect tensile test fracture surface: a) scheme; b) NWC; c) LWC

A similar indication is provided by both the visual and microscopic analyses of the pulled-out Ti6Al4V rebars through the conducted tests. Fig. 7 shows the rebar portion that was bonded to the matrix. The presence of residual matrix materials on the rebar surface, for both the mixtures tested, corroborates the hypothesis of the presence of an irregular dilating fracture interface, drawn by observing the bond stress-slip relationships (Par. 2.3.1). Concerning NWC (Figs. 7a and 7b), the rebar shows some distinct spots, while in the case of LWC (Figs. 7c and 7d) the rebar surface exhibits a sort of microfilm of residual material relatively uniform. On one hand, this aspect seems to affect the bond strength value, which is higher when adhesion regularly involves a larger surface (LWC case). On the other hand, it can be responsible for the local boosts of the softening branch of bond-slip responses in the case of NWC, when adhesion is restricted to discrete areas.
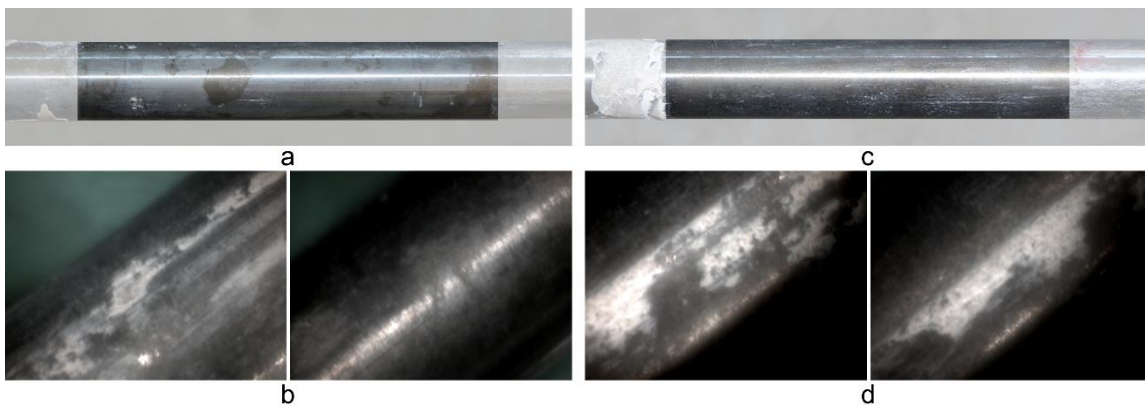

Fig. 7 - - a) visual and b) microscopic analysis of Ti6Al4V bars pulled out from NWC specimens; c) visual and d) microscopic analysis of Ti6Al4V bars pulled out from LWC specimens

2.3.3 Comparison with other reinforcement materials

In this paragraph the attention is focused on the bond strength values obtained from the pull-out test by comparing normalised bond strength values of the tested Ti6Al4V-concrete interface with those reported in the literature for plain rebars of different materials. From the considerable amount of data available for pull-

out tests, only data obtained under similar conditions are selected for comparison, even if some parameters related to the bar surface (e.g. roughness, treatment, finish) are not always available. Although the comparison is far from being complete and exhaustive, at this preliminary step it has been considered essential to assess whether Ti6Al4V-concrete bond performance is comparable to that of other materials used as concrete reinforcement. Data found in the literature are compared to the mean values of the normalised bond strengths obtained from the pull-out tests carried out herein.

Table 4 collects values of bond strength (τ_{max}) and normalised bond strength (τ_{max}^*) with respect to the square root of the concrete strength (f_{cm}) for different rebar materials, plain (P) rebar surface characteristics (possible textures or treatments), roughness (R_y), bond lengths (l_b), and cross-section geometrical details (bar diameter d_s for round bars or sides dimension $a \times b$ for bars with a rectangular cross-section). The same data are reported in the forthcoming Fig. 8, where the normalised bond strengths collected in the literature are compared with those measured here for the Ti6Al4V bars, i.e. 0.29 MPa0.5 for NWC and 0.51 MPa0.5 for LWC (average values). Some of the data collected for ribbed bars, instead, are reported in Table 5 demonstrating that normalised bond strength values for plain rebars are about 20-30% of those related to ribbed rebars (around 0.4-0.5 MPa0.5 for plain rebars and around 2-3 MPa0.5 for ribbed ones). This means that studying the pull-out behaviour of plain rebars can be very useful to better understand the pure pull-out failure mechanism, which represents a considerable percentage of the bond strength and would be overshadowed by the predominant interlocking phenomenon induced by ribs.

Table 4 - Bond strength values comparison for plain rebars

REF.	Rebar Material	Plain rebar - Surface Texture	R_y	τ_{max}	d_s	a	b	l_b	f_{cm}	$\tau *_{max}$
			(μm)	(MPa)	(mm)	(mm)	(mm)	(mm)	(MPa)	(MPa$^{0.5}$)
[25]	Steel	P - smooth	3.1	1.21	16			192	14.4	0.32
	Steel	P - smooth	3.1	1.79	16			192	44	0.27
	Steel	P - sandblast	11.3	2.28	16			192	9	0.76
	Steel	P - heavy sandblast	24.7	3.10	16			192	15	0.80
[22]	Steel	P		1.84	10			125	31.3	0.33
[17]	Steel	P		2.76	12.7			120	27	0.53
	Zinc-coated steel	P		0.92	12.7			120	27	0.18
[6]	Steel	P	13.2	5.26	10			50	61.3	0.67
	Stainless Steel	P	0.4	1.49		4	20	50	59.8	0.19
	Stainless Steel	P	3.0	1.79		4	20	50	59.8	0.23
[23]	Steel	P		2.22	16			115	40.8	0.35
	Aluminium Alloy	P		0.23	16			115	40.8	0.04
[13]	CFRP	Coarse sanded		3.99	8			64.7	52.73	0.55
	CFRP	Fine sanded		2.74	8			40	46.82	0.40
	GFRP	Coarse sanded		3.89	8			55	52.73	0.54
	GFRP	Fine sanded		3.38	8			52.5	52.73	0.47
	Steel	Smooth		1.10	12			60	30.53	0.20
[15]	GFRP	P - Rough		12.50	13.5			81	49	1.79
	GFRP	P - Medium Rough		5.30	10.5			60	41	0.83
	GFRP	P - Smooth		1.20	16			80	45	0.18
	CFRP	P - Rough		11.80	13.5			81	46	1.74
	CFRP	P - Rough		14.00	8			48	41	2.19
	AFRP	P - Rough		10.10	13.5			81	45	1.51

10

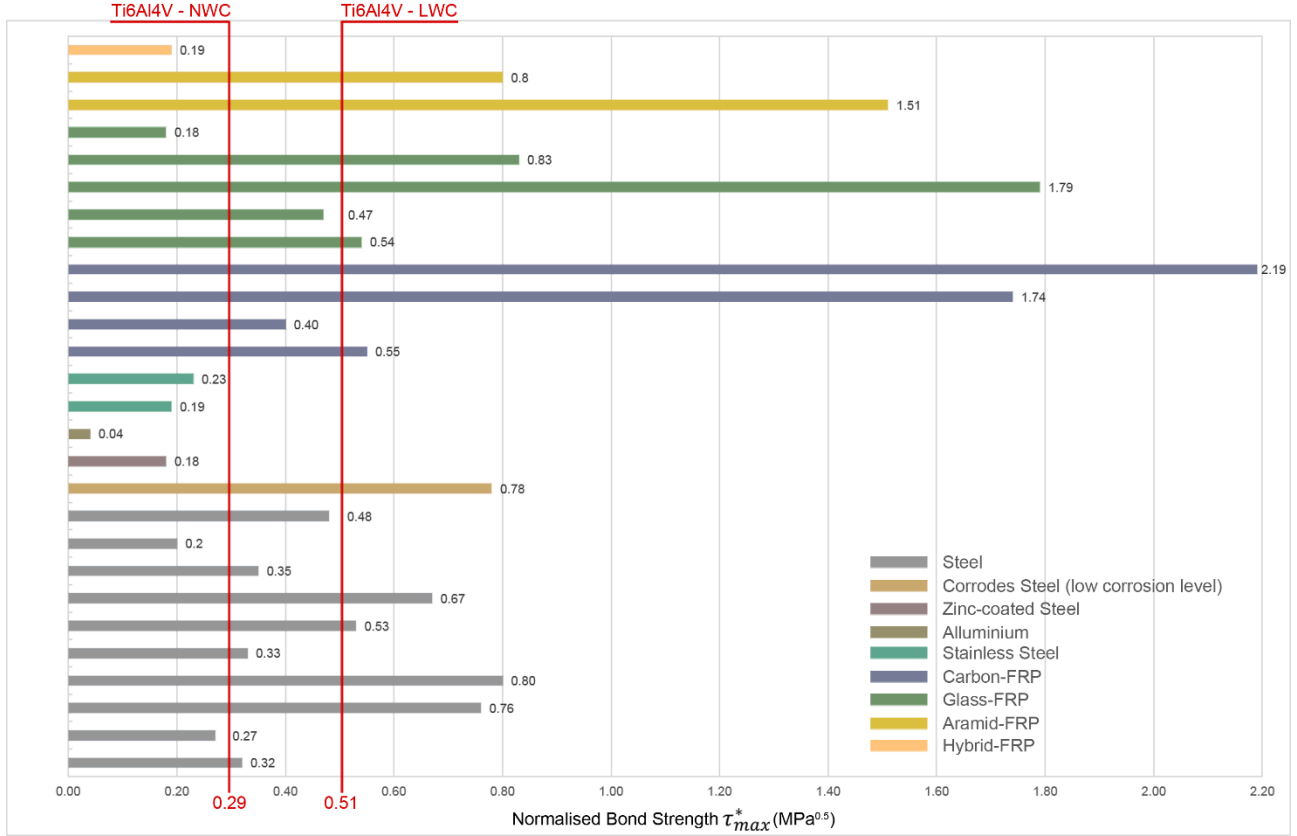| REF.	Rebar Material	Plain rebar - Surface Texture	R_y	τ_{max}	d_s	a	b	l_b	f_{cm}	$\tau *_{max}$
			(µm)	(MPa)	(mm)	(mm)	(mm)	(mm)	(MPa)	(MPa$^{0.5}$)
	AFRP	P - Rough		5.40		8	8	81	45	0.80
	Hybrid FRP	P - Smooth		1.30	8			81	45	0.19
[54]	Steel	P		3.40	12			80	49.6	0.48
	Corroded Steel	P		5.50	12			80	49.6	0.78

Fig. 8 - Bond strength comparison between Ti6Al4V bars and other reinforcement materials with respect to concrete

Table 5 - Bond strength values comparison for ribbed rebars

REF.	Rebar Material	Ribbed rebar	R_y	τ_{max}	d_s	l_b	f_{cm}	$\tau *_{max}$
			(µm)	(MPa)	(mm)	(mm)	(MPa)	(MPa$^{0.5}$)
[23]	Steel	R		20.33	16	115	48.5	2.92
[13]	GFRP	R		14.16	12.7	72.5	52.73	1.95
	Steel	R		8.52	13.3	66.5	30.53	1.54
[54]	Steel	R		12.10	12	80	49.6	1.72
	Corroded Steel	R		11.80	12	80	49.6	1.68
[55]	Steel (CL=0%)	R		14.70	13	37.1	28.3	2.76
	Corroded Steel (CL=2%)	R		15.6	13	38.4	28.3	2.93
	Corroded Steel (CL=5%)	R		10.50	13	36.6	28.3	1.97

By comparing normalised bond strength values obtained for Ti6Al4V rebars and those found in the literature, it has been observed that they are comparable for most of the cases where plain rebars of different materials are used (Table 4 and Fig. 8). In particular, reference values for the bond strength in the case of plain steel rebars can be found in [25], where the influence of various parameters, e.g. surface roughness, bar embedded length, concrete compressive strength, on the bond strength are investigated. Although the surface

roughness of the steel bars tested in [25] is higher (3.1 μm) than that of the tested Ti6Al4V ones (1.6 μm), normalised bond strength is almost the same in the case of Ti6Al4V-NWC interface, i.e. 0.20÷0.35 and 0.29 MPa$^{0.5}$ for Ti6Al4V-NWC. As for Ti6Al4V-LWC interface, instead, the normalised bond strength is 0.51 MPa$^{0.5}$, which is higher than that developed between plain steel rebars without surface treatments reported in [25] and [22]. When sandblast treatments are applied to steel rebars, and thus the surface roughness is sensibly increased, the normalised bond strength significantly grows up to values around 0.8 MPa$^{0.5}$ [25]. Conversely, plain smooth zinc-coated steel reinforcements tested in [17] exhibit lower values of normalised bond strength (0.18 MPa$^{0.5}$) with respect to those resulting from the tests on Ti6Al4V. The same condition can be noticed for bond strengths obtained for stainless steel in [6] (0.19 MPa$^{0.5}$ for R_y=0.4 μm and 0.23 MPa$^{0.5}$ for R_y=3.0 μm), and plain aluminium bars tested in [23] (0.04 MPa$^{0.5}$), For different types of FRP (e.g. Aramid, Glass, Carbon, Hybrid Fibre Reinforced Polymer) reinforcements, a vast amount of results is available in the literature [13], [15], [14]. The normalised bond strength measured with pull-out tests of smooth GFRP reinforcing bars in [15] is 0.18 MPa$^{0.5}$, which is lower than that obtained for Ti6Al4V-NWC and Ti6Al4V-LWC interface. Also in the case of different type of FRP reinforcements, when roughness is augmented by applying surface treatments, the normalised bond strength meaningfully increases up to values around 2-2.5 MPa$^{0.5}$ [13], [15]. Finally, bond strengths for plain rebars pulled out from a cement-based repair mortar (composed by cementitious grout, sand, synthetic resin, silica fume and polyamide fibres) corroded and non-corroded tested in [54], are considered. In this case, the initial bond strength increase induced by corrosion is remarkable, i.e. from 0.48 to 0.78 MPa$^{0.5}$. These last data cannot be directly compared with those obtained in the present work, being the former obtained for a matrix specifically designed for bond improvement and corrosion reduction. However, they are able to outline a sort of general trend for the bond behaviour under increasing corrosion action and thus, increasing Corrosion Level (CL), which is also noticeable from Table 5 for ribbed rebars [54], [55]. Even if, at first, corrosion leads to a not negligible increase of bond strength (especially for plain rebars), eventually it always adversely influences the overall bond performance between rebar and matrix, due to the cracking formation process that it induces caused by the simultaneous reduction of cross section and volumetric expansion of oxides [10]. This constitutes the main reason why other corrosion resistant materials have been largely investigated as possible reinforcement for concrete structures.

In this context, the possibility to use titanium alloy could play an important role as it exhibits an outstanding corrosion resistance [50] and, as demonstrated in this experimental work, bond strength values comparable with that of steel (plain rebars with even higher surface roughness), higher than that of stainless steel (plain flat rebars also when surface roughness is increased) and sensibly greater than that of FRP (plain smooth rebars).

2.4 Hypotheses after Experimental Testing

The analysis of the experimental results has led to formulate some hypotheses to explain the behaviour shown by the Ti6Al4V-concrete interface under pull-out conditions. They are summarised below:

- for plain rebars pulled out from a concrete matrix, interface roughness is originated by defects and by the fracture process itself, and activates a non-negligible interlocking mechanism at microscopic level;
- as a consequence of surface roughness, Ti6Al4V-concrete interface exhibits a frictional dilatant behaviour, responsible for the noticeable residual load capacity shown by all the tests carried out;

- matrix homogeneity in terms of aggregates spatial distribution promotes the development of higher bond strengths at the interface with the rebar.

To verify these hypotheses and enucleate the actual micro-mechanisms contributing to the macroscopic response of the rebar-concrete debonding process, a FE analysis is employed and presented in the next section.

3 Finite Element Analysis of Pull-out test

As reported in the previous section, experimental evidence has led to suppose the development of an interlocking mechanism at the interface, which consequently exhibits a dilatant behaviour. On the other hand, in the case of plain rebars, this behaviour is usually neglected in support of a debonding process governed mainly by adhesion and friction [23], [25]. To investigate further this controversial point, different CZMs have been here employed to model the interface debonding process. The results of the FE analyses reported in this section demonstrate that only by taking into account the dilatant behaviour of the interface, it is possible to replicate the experimental results obtained through pull-out tests. As far as the interface modelling is concerned, the micromechanics-based CZM accounting for damage, friction, interlocking and dilatancy proposed by Serpieri et al. [45] is here adopted and extended.

3.1 Description of the numerical model

The numerical analyses have been carried out with the finite-element code ANSYS R16 [56]. Due to the symmetry of the pull-out problem, a 2D axisymmetric model has been used, even if the specimens used in the tests were cubic. This choice is justified by the availability of experimental evidence confirming that the specimen edges do not give any contribution when specimens are large enough and the failure is provided by a pure pull-out mechanism [24]. Matrix and rebar are discretised by fully integrated 8-node axisymmetric elements, while 6-node quadratic interface elements are used in correspondence of the bar-matrix interface. In its proximity a mesh refinement has been applied, so that elements close to the interface are six times smaller than those on the free edge of the concrete matrix. Geometry (Fig. 9a), interface details and boundary conditions (Fig. 9b), and mesh discretisation (Fig. 9c) of the pull-out FE model are reported in Fig. 9. The interface length is equal to five time the bar diameter, which corresponds to 40 and 80 mm respectively for the $\phi 8$ and $\phi 16$ mm rebars, respectively.
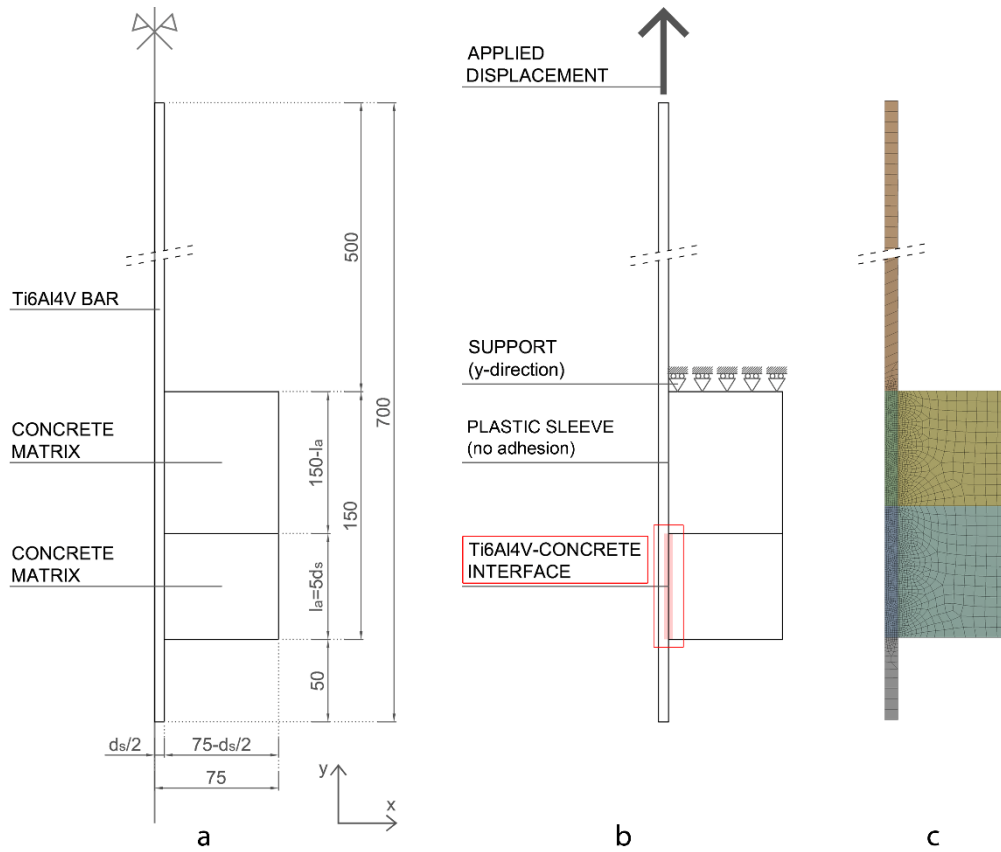
Fig. 9 - FE model: a) geometry; b) interface details and boundary conditions; c) example of mesh discretisation for the case of $\phi16$ mm rebar

Quasistatic nonlinear incremental analyses have been performed applying a prescribed displacement in the *y*-direction at the top of the bar in two load steps. In particular, for the pull-out of $\phi8$ mm rebars, the prescribed final displacement is 12.5 mm while for the $\phi16$ mm ones, the displacement is equal to 25 mm. The first load step (0-5 mm) has been divided in 500 substeps, with constant prescribed displacement increment of 0.01 mm in each substep, in order to obtain a more precise and detailed curve in the linear and post-peak regions of the system response. In the second load step instead (5-12.5 and 5-25 mm for $\phi8$ and $\phi16$ rebars, respectively), the displacement increment in each substep is 0.1 mm. This value is considered sufficient to study the behaviour up to a slip value equal to about 30% of the interface length above which the experimental curves show a gradual decrease that is mostly due to the reduction of the embedment length. This effect cannot be captured with the CZM used here, because the model does not update the pairing of contact surfaces on the interface in the deformed configuration. Moreover, the attention is focused on the crucial mechanisms involved in the debonding process, i.e. adhesion, interlocking and friction, which can be already captured for prescribed displacements considerably lower than the bond length.

The bulk material properties are reported in Table 6 and have been derived from compressive and indirect tensile tests on NWC and LWC and from tensile tests on Ti6Al4V bars. Both concrete and titanium alloy have been modelled through a linear-elastic behaviour, since the stresses in the pull-out tests give negligible damage and plasticity effects.

14

Table 6 - Material properties for the FE analysis

	Density	Isotropic Elasticity		Compressive Yield Strength	Tensile Yield Strength	Compressive Ultimate Strength	Tensile Ultimate Strength
		Young's Modulus	Poisson's Ratio				
	(kg/m³)	(MPa)	(-)	(MPa)	(MPa)	(MPa)	(MPa)
NWC	2325	33885	0.18	-	-	42	1.8
LWC	1735	30400	0.18	-	-	29	1.5
Ti6Al4V	4500	100000	0.36	920	920	-	962

3.2 Bilinear and Exponential CZMs for the interface modelling

The most used cohesive models for the description of debonding/delamination processes employ exponential (Fig. 10a) and bilinear (Fig. 10b) and laws.
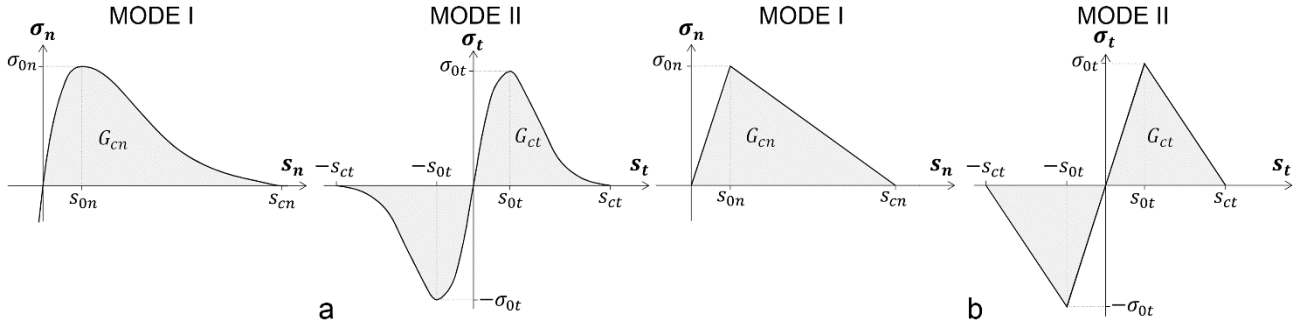

Fig. 10 - a) mode I and mode II exponential CZM laws; b) mode I and mode II bilinear CZM laws

ANSYS R16 [57] provides the formulation of Alfano and Crisfield [33] for the bilinear CZM and the one proposed by Xu and Needleman [35] for the exponential law. These model are directly applicable to the elements used in proximity of the bar-matrix interface. In a first phase of this work, both the bilinear and the exponential laws for interface delamination models have been used in order to understand their advantages and limitations. Starting from these simpler models, it is possible to calibrate the parameters that describe debonding for each fracture mode (mode I – normal; mode II – tangential), i.e. critical energy release rate G_c, maximum cohesive traction σ_0, displacement jump at maximum cohesive traction (s_0) and at complete debonding (s_c). The adopted values of the previous parameters are reported in Table 7 for both the cohesive laws. It is worth underlining that in the case of pull-out mechanism fracture is governed by a mode II fracture behaviour, being the shear forces and the subsequent relative sliding the main factor responsible for the interface failure.

Table 7 - Values of the fracture parameters for Mode I and Mode II

Property		Unit	Value	
			NWC	LWC
Maximum Normal Traction	σ_{0n}	(MPa)	1.00	1.00
Normal Displacement at Maximum Tangential Traction	s_{0n}	(mm)	10^{-4}	10^{-4}
Normal Displacement Jump at Complete Debonding	s_{cn}	(mm)	0.45^{-4}	0.6^{-4}
Maximum Tangential Traction	σ_{0t}	(MPa)	1.85	2.80
Tangential Displacement at Maximum Tangential Traction	s_{0t}	(mm)	0.45	0.64
Tangential Displacement Jump at Complete Debonding	s_{ct}	(mm)	1.00	1.07

3.2.1 Results and discussion

By applying the bilinear and exponential CZMs for the simulation of interface fracture, load-displacement curves have been obtained for the two types of concrete mixture (NWC and LWC) and the two bar diameters tested (ϕ8 and ϕ16 mm). For the sake of brevity, just the result concerning the ϕ16 mm rebar pull-out from

NWC specimens is reported in Fig. 11, where the response until a slip value equal to 10 mm is reported. The other curves exhibit the same qualitative behaviour.
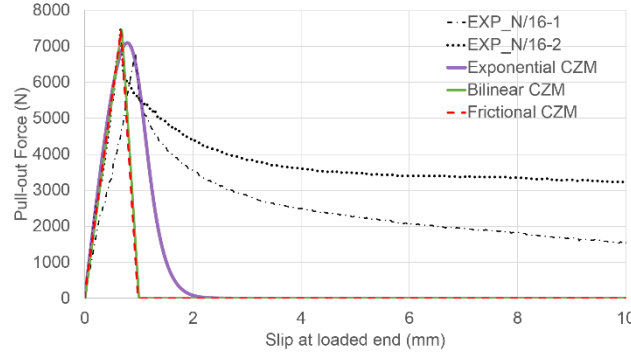

Fig. 11 - ϕ16 mm rebars pull-out from NWC specimens: Comparison between Bilinear (Alfano and Crisfield model [33]), Exponential (Xu and Needleman model [35]), and frictional (Alfano and Sacco model [41]) CZMs and experimental curves

Fig. 11 shows that the two cohesive zone models used, i.e. the bilinear and exponential formulations, can well capture the behaviour of the response curve within the elastic range and, especially in the case of the Alfano and Crisfield (bilinear) model, the first part of the softening curve corresponding to the post-peak sudden drop. However, both of them are unable to capture the residual force obtained from all the experimental curves. This residual force has a significant value, being a non-negligible percentage (around 35% on average) of the peak one. For this reason, a different cohesive model accounting for friction and dilatancy is introduced in the following paragraph. To demonstrate the actual importance of the dilatant behaviour of the interface, Fig. 11 shows also an example of the system response (ϕ16 rebar, NWC) using a CZM accounting for damage and friction, without considering dilatancy. The model proposed by Alfano and Sacco [41], which includes friction, is not able to capture the residual post-peak force, as it happens with the two models considered above. This because the resultant compressive stresses at the bar-matrix interface computed with this model are negligible. Therefore, it can be concluded that friction can play a role only if dilatancy is taken into account.

3.3 Angle-degrading M-CZM accounting for damage, friction and dilatancy for the interface modelling

To simulate the post-peak response during the pull-out tests, but also to support some of the hypotheses made to explain such behaviour, the frictional angle-degrading M-CZM proposed by Serpieri, Alfano and Sacco accounting for the reduction of the inclination angles of elementary planes due to degradation/wear in [45] has been employed and enhanced with a more refined description of the mechanics of wear/degradation, as explained below. The model has been implemented in a user-subroutine (USERCZM) in the FE code ANSYS R16. A brief description of the model is made here, referring to [45] for more details.

3.3.1 Description of the 'enhanced degrading M-CZM'

The angle-degrading M-CZM proposed in [45] is formulated by a micromechanical analysis combining de-cohesion, unilateral contact, friction and dilatancy. It considers a Representative Interface Area (RIA) with asperities according to the scheme previously proposed by Serpieri and Alfano in [43]. In particular, in 2D the RIA consists of three microplanes, one parallel (2) and two inclined (1 and 3) of equal and opposite angles, θ_k, with respect to the interface plane, where k stands for the microplane number. It is assumed that the three microplanes have the same area and that each of them is governed by the interface model proposed by Alfano and Sacco in [41] which combines decohesion and friction. One novel aspect introduced in [45] with respect to the previous model described in [43], consists of accounting for the finite depth, H_N, of the asperities by

16

enforcing equilibrium of the interfacing parts of the RIA in the deformed configuration, so that the progressive reduction of potentially contacting area, due to mode-I opening, is considered. A key feature of the formulation in [45] is the simulation of interface wear by introducing a reduction of the inclination angle of the RIA microplanes, described by Eq. (3):

$$\theta_k = \left(\theta_{k0} - \theta_{kf}\right)e^{-(\zeta_k/\zeta_{k0})} + \theta_{kf} \tag{3}$$

Eq. (3) relates the current value of microplane inclination angle θ_k to the frictional work spent in sliding along the local tangential direction of the kth plane since the beginning of the analysis and given by Eq. (4).

$$\zeta_k = \int_{history} \sigma_{kt} ds_{kf} \tag{4}$$

The quantities θ_{k0}, θ_{kf} and ζ_{k0} define the evolution of the kth microplane degradation. In particular, θ_{k0} is the microplane inclination angle at the beginning of the analysis, θ_{kf} is its value asymptotically approached when ζ_k tends to infinity and ζ_{k0} represents a characteristic energy value controlling the rate of degradation. A scheme of the RIA for the present model is given in Fig. 12.
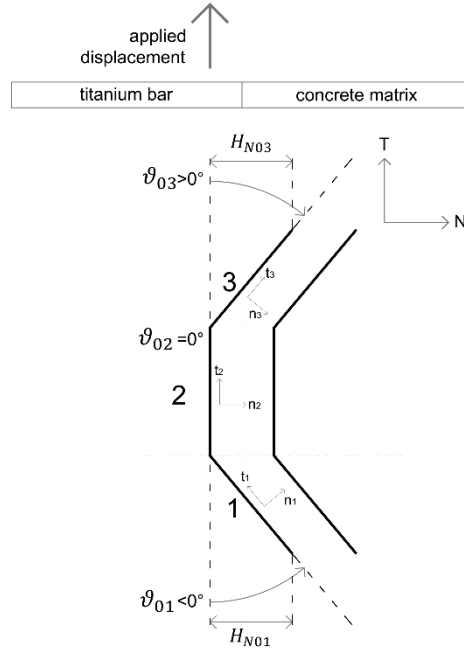

Fig. 12 - RIA scheme

In [45] the asperities depth, H_N, is assumed to be constant during the analysis. The extension of the model proposed in this work, instead, provides for its degradation, consistently with the decrease in the microplane angle. Thus, the law that describes progressive reduction of the asperity depth originated in a microplane k is given by Eq. (5). This law is applied only to microplanes 1 and 3, because $\theta_{20}=\theta_{2f}= 0$.

$$H_{Nk} = H_{N0}\frac{\tan\theta_k}{\tan\theta_{k0}} \tag{5}$$

Another aspect that has been investigated in addition to [43] and [45] concerns the microplanes area. Actually, in [45], the effective initial area fraction $\hat{\gamma}_{0k}$ of the kth microplane is always assumed equal to 1/3, because the RIA is composed of three microplanes with the same area. Conversely, in this work different area fractions for the RIA microplanes are assumed.

Table 8 summarises all the parameters involved in the enhanced degrading M-CZM, with their description and expression where needed.

Table 8 - Enhanced degrading M-CZM input parameters

Parameter	Unit	Expression	Description
G_{cn}	(kJ/m²)	$G_{cn} = \frac{1}{2}\sigma_{0n}s_{cn}$	Fracture Energy Mode I (Normal)
G_{ct}	(kJ/m²)	$G_{ct} = \frac{1}{2}\sigma_{0t}s_{ct}$	Fracture Energy Mode II (Tangential)
σ_{0n}	(MPa)		Maximum Cohesive Traction Mode I (Normal)
σ_{0t}	(MPa)		Maximum Cohesive Traction Mode II (Tangential)
η	(-)	$\eta = 1 - \dfrac{s_{0n}}{s_{cn}} = 1 - \dfrac{s_{0t}}{s_{ct}}$	Coefficient that controls the ratio between the displacement at the completion of debonding and its value at maximum cohesive traction
μ	(-)		Friction Coefficient
$\hat{\gamma}_{01}$	(%)		Initial effective area fraction of microplane 1
$\hat{\gamma}_{02}$	(%)		Initial effective area fraction of microplane 2
$\hat{\gamma}_{03}$	(%)		Initial effective area fraction of microplane 3
θ_{01}	(deg)		Initial inclination angle of microplane 1
θ_{f1}	(deg)		Final inclination angle of microplane 1
ζ_{01}	(kJ/m²)		Characteristic energy value controlling the rate of degradation on microplane 1
θ_{02}	(deg)		Initial inclination angle of microplane 2
θ_{f2}	(deg)		Final inclination angle of microplane 2
ζ_{02}	(kJ/m²)		Characteristic energy value controlling the rate of degradation on microplane 2
θ_{03}	(deg)		Initial inclination angle of microplane 3
θ_{f3}	(deg)		Final inclination angle of microplane 3
ζ_{03}	(kJ/m²)		Characteristic energy value controlling the rate of degradation on microplane 3
H_{N01}	(mm)		Initial depth of asperities on microplane 1
H_{N02}	(mm)		Initial depth of asperities on microplane 2
H_{N03}	(mm)		Initial depth of asperities on microplane 3

3.3.2 Results and discussion

3.3.2.1 Sensitivity analysis and identification

Several sensitivity analyses were performed to evaluate the influence that each model parameter has on the overall system response. After this procedure, the most suitable value of each parameter is identified in order to fit the experimental curves for both NWC and LWC. In particular, sensitivity analyses have been carried out for those parameters mostly affecting the post-peak response. In fact, concerning the linear and the immediate post-peak branches, with the bilinear CZM (Alfano and Crisfield model [33]) it was already possible to capture the maximum cohesive traction and the correspondent slip value. The calibration of these parameters, the fracture energy and the ratio between the slip at maximum traction and the slip at the complete debonding has led to the values for NWC and LWC summarised in the first three rows of Table 9. These parameters are kept constant in all the sensitivity analyses carried out. Notice that, with the enhanced degrading M-CZM it is possible to take the same fracture energy and the same maximum cohesive traction for both modes I and II [43], [44]. This is because the increase of total energy dissipated per unit of new cracked energy with increase in mode II/mode I ratio is the result of the interplay between damage, friction and geometry of the asperities. In other words, the larger the mode II/mode I ratio, the more is the energy dissipated through friction which is added to the share of energy dissipated by loss of cohesion.

In all the following analyses the response of the interface model is evaluated in terms of shear force-slip curves and compared to the obtained experimental results. The enhanced degrading M-CZM input parameters are reported in Table 9 for each sensitivity analysis carried out.

Table 9 - Fixed and variable enhanced degrading M-CZM input parameters for the sensitivity analyses

	Parameter	Unit	Sensitivity to θ_0 Value		Sensitivity to θ_f Value		Sensitivity to ζ_0 Value		Sensitivity to H_{N0} Value	
			NWC	LWC	NWC	LWC	NWC	LWC	NWC	LWC
Fixed	$G_{cn} = G_{ct}$	(kJ/m^2)	0.925	1.50	0.925	1.50	0.925	1.50	0.925	1.50
	$\sigma_{0n} = \sigma_{0t}$	(MPa)	1.85	2.80	1.85	2.80	1.85	2.80	1.85	2.80
	η	(-)	0.55	0.40	0.55	0.40	0.55	0.40	0.55	0.40
	μ	(-)	0.50	0.50	0.50	0.50	0.50	0.50	0.50	0.50
	$\hat{\gamma}_{01}$	(%)	42.5	42.5	42.5	42.5	42.5	42.5	42.5	42.5
	$\hat{\gamma}_{02}$	(%)	15	15	15	15	15	15	15	15
	$\hat{\gamma}_{03}$	(%)	42.5	42.5	42.5	42.5	42.5	42.5	42.5	42.5
Variable	θ_{01}	(deg)	variable	variable	-50	-50	-50	-50	-50	-50
	θ_{f1}	(deg)	0	0	variable	variable	-5	-6	-5	-6
	ζ_{01}	(kJ/m^2)	3.35	3.35	3.35	3.35	variable	variable	1.80	2.50
	θ_{02}	(deg)	0	0	0	0	0	0	0	0
	θ_{f2}	(deg)	0	0	0	0	0	0	0	0
	ζ_{02}	(kJ/m^2)	0	0	0	0	0	0	0	0
	θ_{03}	(deg)	variable	variable	50	50	50	50	50	50
	θ_{f3}	(deg)	0	0	variable	variable	5	6	5	6
	ζ_{03}	(kJ/m^2)	3.35	3.35	3.35	3.35	variable	variable	1.80	2.50
	H_{N01}	(mm)	0.015	0.015	0.015	0.015	0.015	0.015	variable	variable
	H_{N02}	(mm)	0.015	0.015	0.015	0.015	0.015	0.015	variable	variable
	H_{N03}	(mm)	0.015	0.015	0.015	0.015	0.015	0.015	variable	variable

The following sensitivity analyses have been carried out for the case of ϕ16 mm rebar for both NWC and LWC. As a final step, the values of the parameters obtained from the identification procedure are then introduced in the FE models with ϕ8 mm rebars, and the resulting numerical responses are compared with the experimental ones. This last step is intended for the overall validation of the present modelling strategy based on the enhanced degrading M-CZM.

In order to account for the effective bond length at each analysis step, the numerical reaction force is scaled by adopting a corrective factor taking into account the effective bond zone containing asperities which still remain in contact with the surrounding concrete surface and which, as such, contribute to the bond by interlocking. This zone is depicted in red in Fig. 13 showing the bar configuration at the beginning of the pull-out (Fig. 13a) and at a subsequent i-th generic step (Fig. 13b). As Fig. 13a shows, the surface of the bottom portion of the bar which is placed in the exterior of the concrete specimen during curing, and consequently, it is free from asperities (which we recall are essentially made of cement paste particles adhering to the bar). This bond-free surface, which is not affected by interlocking, is accordingly depicted in grey. In a similar way, once the bar has displaced to the right, the part of the bar which has moved inside the plastic sleeve also gives no interlocking contribution, and, as such, is depicted again in grey in Fig. 13b. It is thus recognised that, overall, in the true experiment, bar sliding reduces the surface of the red region by the length ratio: $(l_b - s_i)/l_b$, where l_b is the length of the initial embedded bar and s_i is the slip value at the i-th generic time step. To address this reduction, which is not accounted for in the FE model, the corrected value of the pull-out force at the i-th time step, $F_{P,i}$, is correlated to the corresponding value of the numerically computed pull-out force, $F_{num,i}$, as follows:

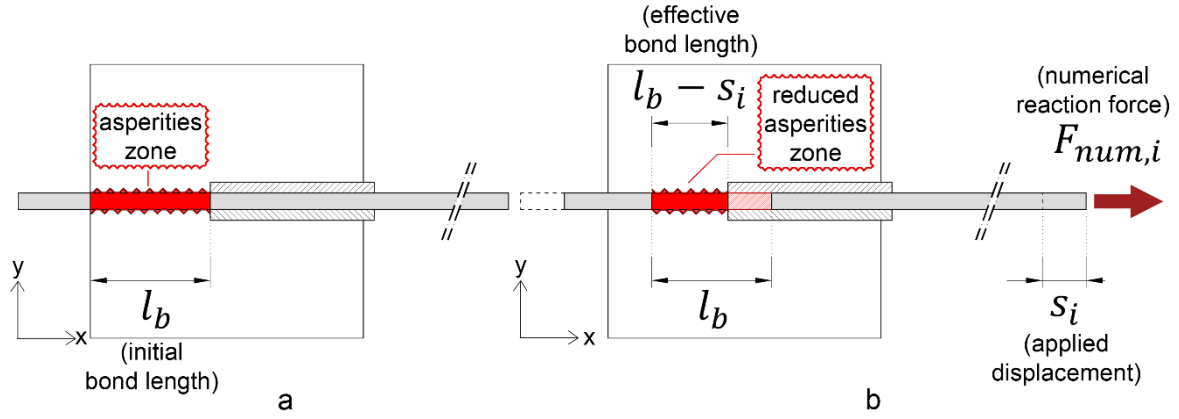$$F_{P,i} = F_{num,i} \frac{l_b - s_i}{l_b}. \tag{6}$$

Fig. 13 - a) Initial configuration with the full bond length interested by the presence of the asperities; b) effective bond length and reduced asperities zone at step i of the analysis

A preliminary analysis identified the percentage of area of inclined planes ($\hat{\gamma}_{01} + \hat{\gamma}_{03}$) over the total RIA area. The best correlation was found for 85% (see Table 9). Thus, this value has been kept fixed for all the following sensitivity analyses.

Sensitivity to initial microplanes inclination angle and identification

Firstly, the attention has been focused on the influence of the initial inclination angle of the microplanes, considering the final one equal to zero. In particular, the angle tested for sensitivity is the modulus $\theta_0 = \theta_{01} = -\theta_{03}$, of the inclined microplanes. The enhanced degrading M-CZM input parameters for the sensitivity analysis to θ_0 are reported in the correspondent column of Table 9, while the results are presented in Figs. 14a and 14b for NWC and LWC, respectively.
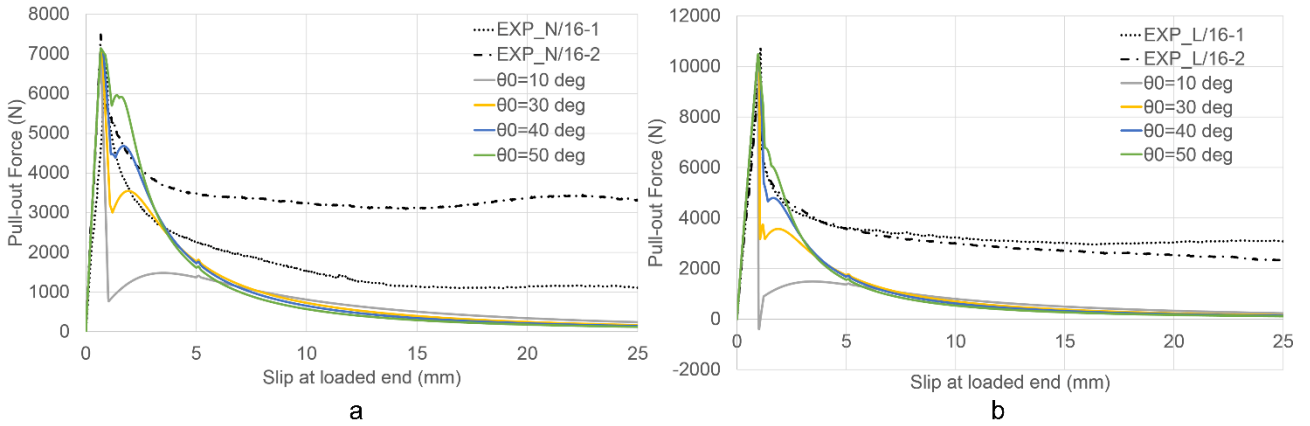

Fig. 14 - Sensitivity to θ_0: a) NWC; b) LWC

From Fig. 14 it is possible to observe that θ_0 influences the residual pull-out force value after the sudden drop caused by the partial loss of adhesion. Starting from this value the pull-out force tends to increase again, reaching a local maximum and, afterwards it decreases according to the exponential degradation law for θ and tends to zero. This last aspect clearly does not represent the real system behaviour, which exhibits a significant residual value of the pull-out force. For both NWC (Fig. 14a) and LWC (Fig. 14b) a suitable initial microplane inclination angle value can be chosen between 40 deg and 50 deg. A value of 50 deg has been adopted for the following analyses. It is shown below that an improved correlation with the shape of the experimental curve can be obtained by calibrating the parameter $\zeta_{01} = \zeta_{03}$.

<u>Sensitivity to final microplanes inclination angle and identification</u>

The second parameter considered in the sensitivity analysis is the final microplanes inclination angle. Also in this case the angle that has been varied is $\theta_{f1}=-\theta_{f3}$, whose modulus is referred to as θ_f, while $\theta_{f2}=0$. The column entitled 'sensitivity to θ_f' of Table 9 reports the enhanced degrading M-CZM input parameters in this sensitivity analysis, whose results are shown in Fig. 15.
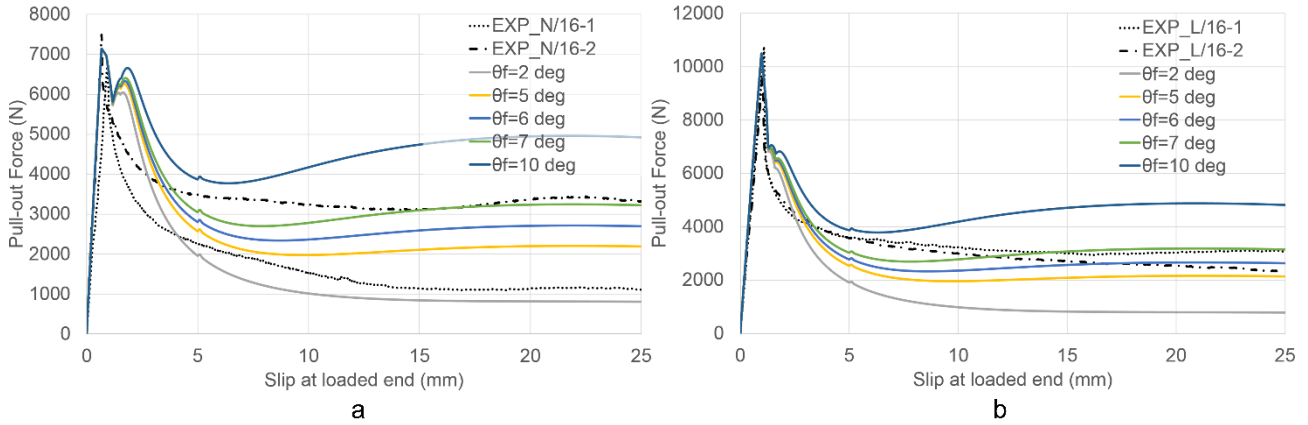

Fig. 15 - Sensitivity to θ_f: a) NWC; b) LWC

By keeping fixed the initial microplane inclination angle and varying the final one, FE analyses provide the results presented in Figs. 15a and 15b for NWC and LWC, respectively. It is possible to notice that θ_f mostly affects the system response starting from the second local maximum identified also in the previous graph (Fig. 14). By increasing θ_f, the pull-out force value tends to be higher, making possible to identify the final inclination angle that best fits the residual pull-out force value obtained from the experimental investigation. Fig. 15a shows the results obtained for NWC, where a θ_f value of about 5 deg seems to be a good compromise among the two experimental curves, which actually exhibit a significant scatter. In the case of LWC (Fig. 15b) the final microplane inclination angle value that better represent the experimental curves is around 6 deg. These values are thus adopted for the following analyses.

<u>Sensitivity to characteristic energy value and identification</u>

The influence of the characteristic energy value ζ_0 is assessed in this paragraph. Afterwards, its value for NWC and LWC is found through the identification procedure. The enhanced degrading M-CZM input parameters for the sensitivity analysis to ζ_0 are summarised in the respective column of Table 9, while the results of the analyses are shown in Figs. 16a and 16b for NWC and LWC.

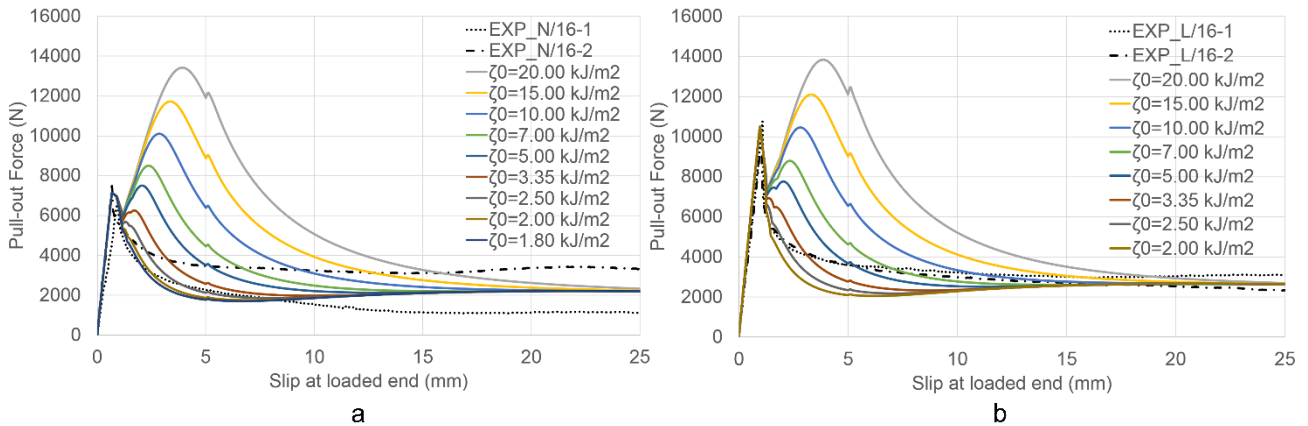Fig. 16 - Sensitivity to ζ_0: a) NWC; b) LWC

The parameter ζ_0 strongly influences the shape of the system response curve in the post-peak area. From Fig. 16, it is possible to observe that for higher values, after the post-peak drop, the pull-out force increases dramatically up to a second local (or global) maximum. This appears to be consistent with the physical meaning of ζ_0 which represents the energy value through which the RIA microplanes degrade. To further investigate this process, the evolution of damage on each microplane is monitored by evaluating the damage variable, D_k, according to Eq. (7) [43], [45]:

$$D_k = \max\left\{0, \min\left\{1, \frac{\beta_k}{\eta(1-\beta_k)}\right\}\right\} \tag{7}$$

with the term β_k given by Eq. (8) [43], [45]:

$$\beta_k = \max_{history}\sqrt{\left(\frac{\langle s_{kn}\rangle_+}{s_{0n}}\right)^2 + \left(\frac{s_{kt}}{s_{0t}}\right)^2} \tag{8}$$

where $\langle s_{kn}\rangle_+$ denotes the positive part of $\langle s_{kn}\rangle$ and the symbol $\langle\cdot\rangle$ represents the Macaulay brackets.

By referring to the curve with ζ_0=5 kJ/m^2, the damage variable trend is tracked by evaluating its value in correspondence of the critical substeps of loadstep 1 (Figs. 17a and 17b) and loadstep 2 (Figs. 17c and 17d) of the analysis.
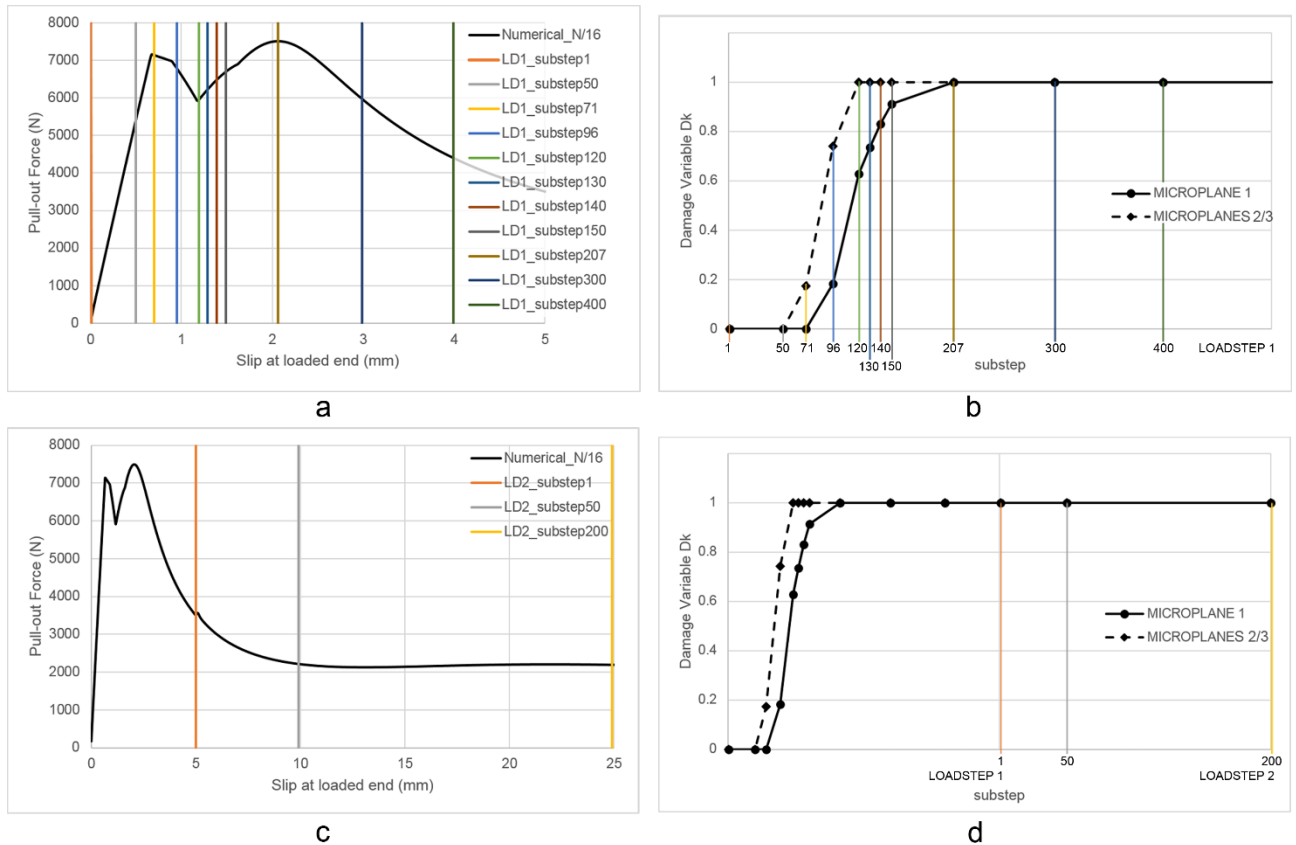
a

b

c

d

Fig. 17 - a) critical substeps of loadstep 1; b) damage variable trend during loadstep 1; c) critical substeps of loadstep 2; d) damage variable trend during loadstep 2

A scheme of the progressive loss of adhesion on the three microplanes considered is reported in Fig. 18. At the beginning, there is complete adhesion at the interface (Fig. 18a). Then, the force drop after the pull-out force strength corresponds to the breakage of the microplanes 2 and 3 (Fig. 18b). At this stage, there still is adhesion on microplane 1. This promotes a new increasing in the pull-out force until a second maximum, which can be either local or global depending on the value of ζ_0. Afterwards, adhesion is lost also on

microplane 1 (Fig. 18c), thus the pull-out force starts to decrease gradually according to the exponential law of the characteristic energy value. The higher the parameter ζ_0 is, the more energy is associated with the fracture of the RIA microplanes, resulting in response curves characterised by 'bumps' in correspondence of the fracture of each microplane.
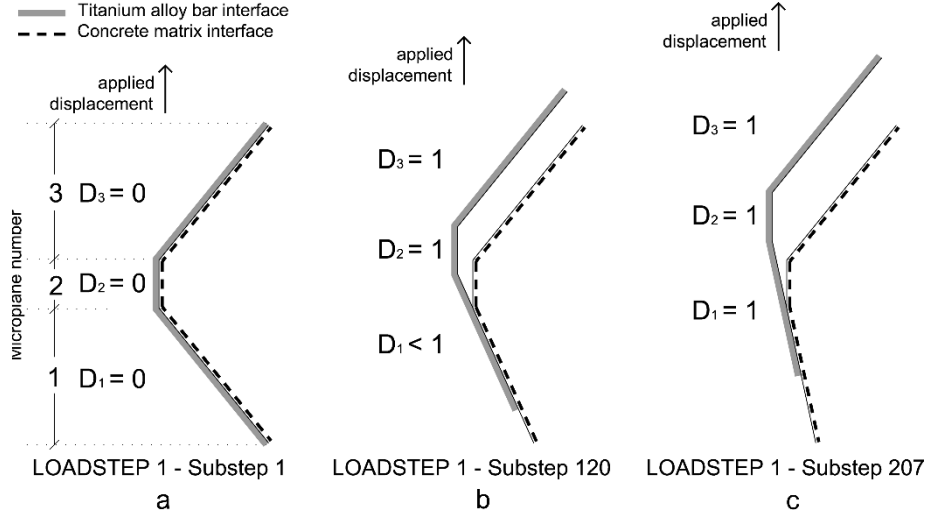

Fig. 18 - Progressive loss of adhesion on the microplanes during loadstep 1: a) substep 1; b) substep 120; c) substep 207

The decomposition of each point of the interface into a certain number of elementary planes allows for the simulation of the fracture process in a progressive way. This seems to be consistent with the experimental curves, suggesting that the interface degradation does not occur suddenly after the peak stress and does not involve simultaneously the whole interface, yet it is a gradual process, activated all through the curve ranging from the peak stress till complete pull-out, and makes the pull-out force slowly decrease to a residual value. In the numerical models, for both NWC and LWC, this behaviour is essentially governed by the parameter ζ_0, whose value is identified in order to match the curve shape. In particular, for NWC $\zeta_0=1.80$ kJ/m^2 (Fig. 16a), while for LWC$\zeta_0=2.50$ kJ/m^2 (Fig. 16b).

Sensitivity to asperities depth and identification

The last parameter whose influence has been investigated is the initial asperity depth H_{N0}. The presented model accounts for its degradation consistently with the microplane inclination angle decreasing law, thus the input parameter H_{N0} refers to its initial value. Figs. 19a and 19b show the results of the sensitivity analysis to H_{N0} for NWC and LWC, which has been carried out by adopting the enhanced degrading M-CZM set of parameters values collected in the last two columns of Table 9.
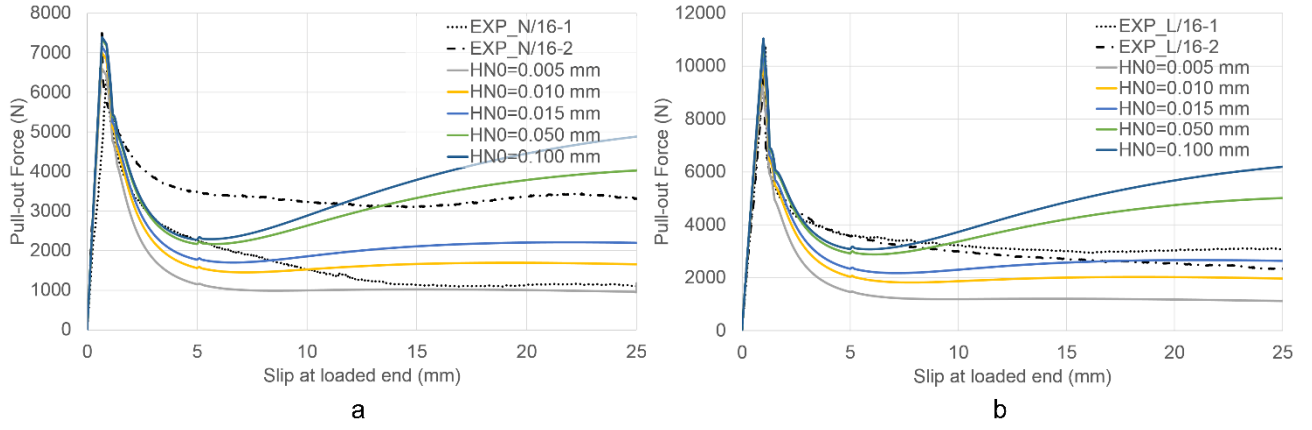
Fig. 19 - Sensitivity to H_{N0}: a) NWC; b) LWC

Fig. 19 shows that the initial asperities depth slightly influences the force peak value in the linear branch, while it affects more significantly the final part of the curve. If H_{N0} is sufficiently high, it is possible to observe that the pull-out force starts to increase with growing slip values. Conversely, the experimental curves show a gradual decreasing trend of the pull-out force after the post-peak zone. This appears to be consistent with lower values of H_{N0}, which, moreover, are of the same magnitude of the range of asperities heights observed by SEM analyses (i.e. approximately 10-15 μm, see Fig. 5). SEM analyses can be seen as a valid tool to measure the 'scale of the problem', and such a scale turns out to be consistently confirmed by the sensitivity FE analyses. In this respect, it is worth recalling that SEM observations provide information about both the range of interface dilation and the range of asperities height originated by residual concrete material remaining attached to the bar surface.

The identification procedure carried out after the sensitivity analysis of each parameter provided the values summarised in Table 10.

Table 10 - Identified values of the enhanced degrading M-CZM input parameters

Parameter	θ_{01}	θ_{f1}	ζ_{01}	θ_{02}	θ_{f2}	ζ_{02}	θ_{03}	θ_{f3}	ζ_{03}	H_{N01}	H_{N02}	H_{N03}
	(deg)	(deg)	(m²/kJ)	(deg)	(deg)	(m²/kJ)	(deg)	(deg)	(m²/kJ)	(mm)	(mm)	(mm)
NWC	-50	-5	1.80	0	0	0	50	5	1.80	0.015	0.015	0.015
LWC	-50	-6	2.50	0	0	0	50	6	2.50	0.015	0.015	0.015

Figs. 20a and 20b show the comparison between numerical and experimental curves for the ϕ16 mm rebars in the cases of NWC and LWC respectively.
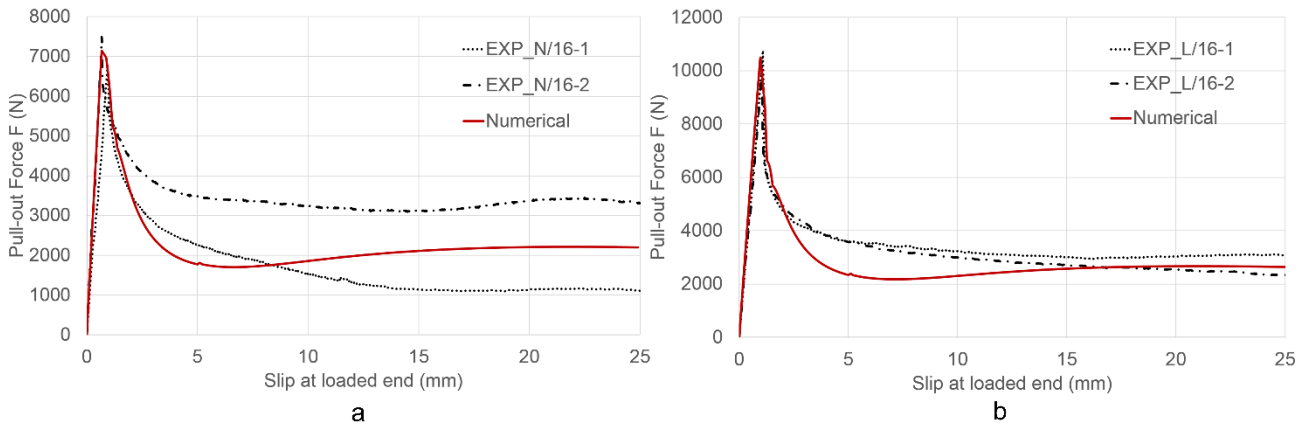

Fig. 20 - Numerical-experimental comparison: a) ϕ16 rebar, NWC; b) ϕ16 rebar, LWC

Fig. 20 demonstrates that the enhanced degrading M-CZM is able to overcome the biggest limitation shown by the bilinear and exponential cohesive models, namely the impossibility to capture the residual force at the end of the post-peak branch. Instead, the shape of the post-peak curve is well captured by using this cohesive model able to account for damage, friction, interlocking and dilatancy. In addition, the introduction in the model of the asperities depth degradation made it possible to avoid the increasing trend of the pull-out force with growing slip values, which can be noticed in the following Fig. 21. This is shown, in particular, for the case of the $\phi 16$ mm bars embedded in LWC, employing the parameters in Table 10. It is possible to see the difference between the results obtained by using the M-CZM formulation by Serpieri et al. [45] and those obtained by the enhanced degrading M-CZM here proposed. Since in the basic angle-degrading model (M-CZM) [45] the asperities have unmodifiable height and only the angle degrades, when sufficiently high slip values are reached, the force increases again deviating from the horizontal plateau. On the contrary, the enhanced degrading M-CZM permits, by properly setting the material parameters, to make the pull-out force decrease to the residual horizontal plateau, a feature found in all experimental force-slip curves. In general, the numerical curves exhibit a hardening-like shape, which is essentially originated by interlocking and depends on the asperities depth. The sensitivity analyses reported herein show that this stress recovery is mitigated by increasing the crushability of asperities which is controlled by parameters θ_0, ζ_k, and H_{N0} and show that this effect is maximum when the asperities height is held constant, as shown by Fig. 21. This numerically predicted hardening-like effect, in some part, can be also detected in some of the experimental test results (Figs. 2 and 3) when sufficient slip is mobilised.
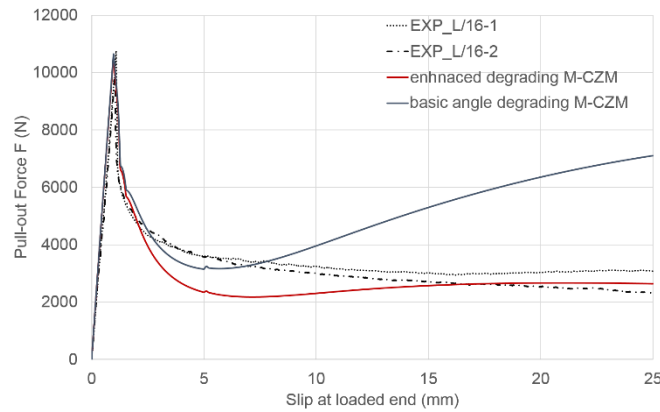

Fig. 21 - Comparison between basic angle-degrading M-CZM [45] and enhanced degrading M-CZM

It should be also remarked that, although numerical and experimental curves do not achieve a perfect agreement by using the enhanced degrading M-CZM, pull-out tests usually exhibit a significant scatter, especially in terms of residual force value. This makes it more important to capture and reproduce the physics behind the phenomenon than the precise force values, and, in this respect, the methodology herein proposed provides encouraging results.

3.3.2.2 Validation of the enhanced degrading M-CZM

The sensitivity analyses so far described have permitted to identify the model parameters giving optimal correlation with the pull out tests executed on $\phi 16$ mm rebars. As conclusive 'litmus' step, FE simulations are carried out using the same parameters of Table 10 resulting from the calibration on tests with $\phi 16$ mm bars, for the tests with $\phi 8$ mm rebar inclusive of both NWC and LWC matrices (Figs. 22a and 22b).
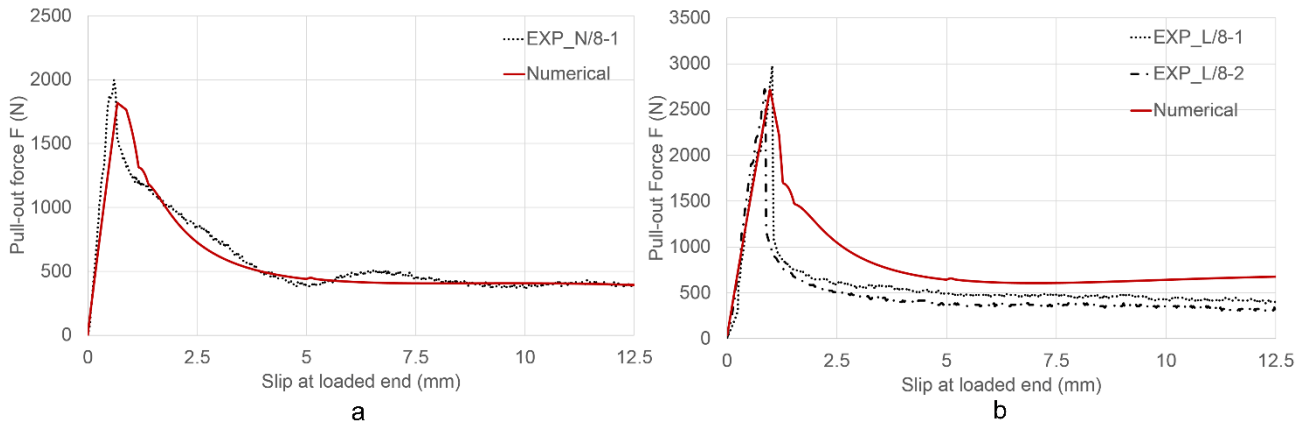
Fig. 22 - Numerical-experimental comparison: a) ϕ8 rebar, NWC; b) ϕ8 rebar, LWC

Figs. 22a and 22b show that good agreement between numerical and experimental curves is still achieved, thus confirming the general validity of the proposed modelling strategy for the characterisation of the bond mechanics in plain bars. In other words, once the parameters are identified for a certain concrete batch, they can be introduced in a different geometrical model, leading to reasonable force-slip response curves.

4 Conclusions

The Ti6Al4V-concrete interface has been studied in the present work, both experimentally and numerically. Bond stress-slip relationships were extracted from pull-out tests conducted on ϕ8 and ϕ16 mm Ti6Al4V bars from Normal (NWC) and Light-Weight Concrete (LWC) specimens. They exhibit the typical pull-out behaviour that reflects three mechanisms, i.e. chemical adhesion, friction and mechanical interlocking. Noteworthy, despite only plain bars have been tested in this study, visual and microscopic analyses of bar surfaces, sampled after pull-out tests, showed reasonable hints for the presence of cement particles adhering to the plain bar surface and subject to crushing during the pull-out test, which may be identifiable, to some degree, as asperities. The presence of these asperities could explain to the authors also several features of the obtained bond-slip diagrams, such as evidences of non-negligible interlocking and dilatancy phenomena, which could not be justified by assuming ideally smooth bars. Moreover, SEM analyses of the bar-matrix interface after a slip equal to 55% of the bond length confirmed the assumed dilatant behaviour, providing also the problem 'scale' through the measure of the separation at the interface, whose magnitude is around 10-15 µm.

Experimental pull-out tests were then used to assess the bond strength between the two materials. In particular, it has been found that the bond strength between the titanium alloy used (Ti6Al4V) and concrete is similar or even higher than the bond strength between concrete and other materials widely used as reinforcement. In fact, the Ti6Al4V-concrete bond strength is similar to that of plain, smooth or even slightly sandblasted steel bars, whereas it is higher than that for stainless steel plain rebars (with greater roughness) and plain, smooth FRP bars. Tests provided another remarkable result in terms of bond strength: the comparison between NWC and LWC shows that in the first case the developed bond strength is significantly lower (about 40%). Both the visual and microscopic analyses of the pulled-out bars revealed the presence of a uniform layer of residual matrix materials in the case of LWC; conversely sparse spots are clearly distinguishable in the case of NWC. This evidence and the observation of the specimen fracture surface, have led to formulate the hypothesis that the higher performance of bond in LWC is ascribable to a much more

uniform asperity degradation along the rebar-concrete interface, i.e. a homogeneous physical aggregate distribution improves the bond strength.

To demonstrate and simultaneously better investigate the physics behind the pull-out mechanism, a FE model has been employed, simulating the interfacial failure through CZMs. Firstly, bilinear [33] and exponential [35] CZMs, two of the most used ones, have been used in the FEA, leading to good agreement between experimental and numerical responses in the range of the linear and immediate post-peak branch of the curves. However, in both cases the resulting force vanishes after the slip value at the completion of debonding, neglecting its residual value. The same behaviour has been observed by using the CZM accounting for damage and friction proposed by Alfano and Sacco [41]. To overcome this limitation, the dilatant behaviour of the interface, assumed after experimental evidence, has been implemented by using the angle-degrading M-CZM proposed by Serpieri et al. in [45], accounting for damage, friction, mechanical interlocking and wear. In the angle-degrading M-CZM, a representative interface area is divided into three microplanes characterised by an inclination angle and a finite depth with respect to the interface plane. In the present work the angle-degrading model has been investigated in further detail by considering different area fraction for the three microplanes and, most importantly, an enhancement of this model has been proposed and validated. The enhancement consists of the due account of the reduction of the asperities depth, consistently with the microplanes angle degradation due to interface wear. This novel feature, in fact, is responsible for non-negligible differences in the mechanical behaviour of the interface and allowed for a more accurate description of the force decay to a residual horizontal plateau. With this model, here denominated 'enhanced degrading M-CZM', sensitivity analyses have been carried out in order to understand the influence of each significant parameter. Thereafter, to fit the experimental curves, an identification procedure has been performed, leading to two optimal set of material interface parameters best fitting the tests with NWC and LWC, respectively, employing ϕ16 Ti6Al4V rebars. Finally, validation of the M-CZM-based modelling strategy herein proposed for the numerical-experimental characterisation of rebar bond behaviour is carried out by applying the sets of interface material parameters to simulate the tests with ϕ8 bars, achieving satisfactory agreement between experimental and numerical curves. Overall, the proposed combined experimental-numerical approach, based on multiplane cohesive-zone modelling, appears to be a viable strategy to investigate the pull-out mechanisms originated in plain bars when the presence of micro-defects triggers non-negligible dilatancy.

As very few experiments on the bond behaviour of unconventional titanium reinforcement can be currently found in the literature, even in presence of a limited number of experiments, the results obtained in this work provide information useful for those particular design problems in which titanium can be considered a valid potential reinforcement for RC, i.e. when structures are exposed to aggressive environments and durability is crucial enough to justify high costs.

Concerning possible future developments overcoming some of the limits of the present study, from the experimental point of view, enlarging the specimens sample could provide a broader database of pull-out response curves thus permitting a statistical quantification of the experimental scattering which has not been carried out herein. As a second possible direction, tests involving durability should be performed in order to actually measure the contribution of the outstanding corrosion resistance of titanium on the bond strength performance over time. From the numerical point of view, instead, use of a 3D CZM, such as the 3D M-CZM formulation proposed in [46], accounting for damage, friction, mechanical interlocking and dilatancy could

give more accurate results, and also offer the possibility to study problems with different types of reinforcement not necessarily characterised by a straight geometrical configuration (e.g. fibres of different geometry).

Authors' contribution. SL conceived the combined experimental and numerical research program, identifying the problem under attention. DM carried out the experimental tests under the supervision of SL. DM extended and implemented the enhanced degrading M-CZM formulation under the supervision of GA and RS. The numerical modelling has been carried out by DM, under the supervision of all the other authors. Formulation of the hypotheses, discussion of the results, and manuscript drafting have been carried out by all the authors, with the main contribution of DM for manuscript writing.

References

1. Söylev TA, Richardson MG. 2008 Corrosion inhibitors for steel in concrete: State-of-the-art report. *Constr. Build. Mater.* **22**, 609–622. (doi:10.1016/j.conbuildmat.2006.10.013)
2. Cheng A, Huang R, Wu JK, Chen CH. 2005 Effect of rebar coating on corrosion resistance and bond strength of reinforced concrete. *Constr. Build. Mater.* **19**, 404–412. (doi:10.1016/j.conbuildmat.2004.07.006)
3. Dong S, Zhao B, Lin C, Du R, Hu R, Zhang GX. 2012 Corrosion behavior of epoxy/zinc duplex coated rebar embedded in concrete in ocean environment. *Constr. Build. Mater.* **28**, 72–78. (doi:10.1016/j.conbuildmat.2011.08.026)
4. Kepler JL, Locke CE. 2000 Evaluation of Corrosion Protection Methods for Reinforced Concrete Highway Structures. *Corrosion* , 231.
5. Ahlborn T, DenHartigh T. 2002 A Comparative Bond Study of Stainless Steel Reinforcement in Concrete.
6. Ertzibengoa D, Matthys S, Taerwe L. 2012 Bond behaviour of flat stainless steel rebars in concrete. *Mater. Struct. Constr.* **45**, 1639–1653. (doi:10.1617/s11527-012-9862-x)
7. Bank LC, Campbell TI, Dolan CW. 2003 Guide for the Design and Construction of Concrete Reinforced with FRP Bars Reported by ACI Committee 440. *Concrete* , 1–42. (doi:10.1061/40753(171)158)
8. Uomoto T, Mutsuyoshi H, Katsuki F, Misra S. 2002 Use of Fiber Reinforced Polymer Composites as Reinforcing Material for Concrete. *J. Mater. Civ. Eng.* **14**, 191–209. (doi:10.1061/(ASCE)0899-1561(2002)14:3(191))
9. Urbanski M, Lapko A, Garbacz A. 2013 Investigation on concrete beams reinforced with basalt rebars as an effective alternative of conventional R/C structures. *Procedia Eng.* **57**, 1183–1191. (doi:10.1016/j.proeng.2013.04.149)
10. Cairns J, Du Y, Law D. 2006 Residual bond strength of corroded plain round bars. *Mag. Concr. Res.* **58**, 221–231. (doi:10.1680/macr.2006.58.4.221)
11. ACI Committee 408. 2003 ACI 408R-03 Bond and Development of Straight Reinforcing Bars in Tension. *Am. Concr. Inst.* , 1–49.
12. Angst UM *et al.* 2017 The steel–concrete interface. *Mater. Struct. Constr.* **50**. (doi:10.1617/s11527-017-1010-1)
13. Antonietta Aiello M, Leone M, Pecce M. 2007 Bond Performances of FRP Rebars-Reinforced Concrete. *J. Mater. Civ. Eng.* **19**, 205–213. (doi:10.1061/(ASCE)0899-1561(2007)19:3(205))
14. Baena M, Torres L, Turon A, Barris C. 2009 Experimental study of bond behaviour between concrete and FRP bars using a pull-out test. *Compos. Part B Eng.* **40**, 784–797. (doi:10.1016/j.compositesb.2009.07.003)
15. Achillides Z, Pilakoutas K. 2004 Bond behavior of fiber reinforced polymer bars under direct pullout conditions. *J. Mater. Civ. Eng.* **4**, 173–181. (doi:10.1061/(ASCE)1090-0268(2004)8:2(173))

16. Treece RA, Jirsa JO. 1989 Bond strength of epoxy-coated reinforcing bars. *ACI Mater. J.* **86**, 167–174. (doi:10.14359/2341)

17. Mo YL, Chan J. 1996 Bond and Slip of Plain Rebars in Concrete. *J. Mater. Civ. Eng.* **8**, 208–211. (doi:10.1061/(ASCE)0899-1561(1996)8:4(208))

18. Yeih W, Huang R, Chang JJ, Yang CC. 1997 Pullout test for determining interface properties between rebar and concrete. *Adv. Cem. Based Mater.* **5**, 57–65. (doi:10.1016/S1065-7355(96)00004-1)

19. Diab AM, Elyamany HE, Hussein MA, Al Ashy HM. 2014 Bond behavior and assessment of design ultimate bond stress of normal and high strength concrete. *Alexandria Eng. J.* **53**, 355–371. (doi:10.1016/j.aej.2014.03.012)

20. Annapoorna GV, Suresh S. 2017 Experimental Study on Bond Behavior of Reinforcing Bars in Plain and Fiber Reinforced Concrete. *Int. J. Adv. Mech. Civ. Eng. ISSN 2394-2827* **4**, 83–86.

21. Seara-Paz S, González-Fonteboa B, Eiras-López J, Herrador MF. 2014 Bond behavior between steel reinforcement and recycled concrete. *Mater. Struct.* **47**, 323–334. (doi:10.1617/s11527-013-0063-z)

22. Anwar Hossain KM. 2008 Bond characteristics of plain and deformed bars in lightweight pumice concrete. *Constr. Build. Mater.* **22**, 1491–1499. (doi:10.1016/j.conbuildmat.2007.03.025)

23. Guohua Xing, Cheng Zhou, TaoWu and BL. 2015 Experimental study on bond behavior between Plain Reinforcing Bars and concrete. *Adv. Mater. Sci. Eng.* **18**, 745–752. (doi:10.1016/j.conbuildmat.2004.04.026)

24. Lundgren K. 2005 Bond between ribbed bars and concrete. Part 1: Modified model. *Mag. Concr. Res.* **57**, 371–382. (doi:10.1680/macr.2005.57.7.371)

25. Feldman LR, Bartlett FM. 2005 Bond Strength Variability in Pullout Specimens with Plain Reinforcement. *ACI Struct. J.* **102**, 860–867. (doi:10.14359/14794)

26. CEB-FIP Report. 2000 Bond of reinforcement in concrete: State of the art. *FIB Bull. 10* , 434. (doi:10.1680/macr.11.00091)

27. Schwalbe K-H, Scheider I, Cornec A. 2013 *Guidelines for Applying Cohesive Models to the Damage Behaviour of Engineering Materials and Structures*. Springer-Verlag Berlin Heidelberg. (doi:10.1007/978-3-642-29494-5)

28. Dugdale DS. 1960 Yielding of steel sheets containing slits. *J. Mech. Phys. Solids* **8**, 100–104. (doi:10.1016/0022-5096(60)90013-2)

29. Barenblatt GI. 1962 The Mathematical Theory of Equilibrium Cracks in Brittle Fracture. *Adv. Appl. Mech.* **7**, 55–129. (doi:10.1016/S0065-2156(08)70121-2)

30. Hillerborg A, Modéer M, Petersson PE. 1976 Analysis of crack formation and crack growth in concrete by means of fracture mechanics and finite elements. *Cem. Concr. Res.* **6**, 773–781. (doi:10.1016/0008-8846(76)90007-7)

31. Park K, Paulino GH. 2013 Cohesive Zone Models : A Critical Review of Traction-Separation Relationships Across Fracture Surfaces. *Appl. Mech. Rev.* **64**, 20. (doi:10.1115/1.4023110)

32. Alfano G. 2006 On the influence of the shape of the interface law on the application of cohesive-zone models. *Compos. Sci. Technol.* **66**, 723–730. (doi:10.1016/j.compscitech.2004.12.024)

33. Alfano G, Crisfield MA. 2001 Finite element interface models for the delamination analysis of laminated composites: \mboxMechanical and computational issues. *Int. J. Numer. Meth. Eng.* **50**, 1701–1736.

34. Allix O, Corigliano A. 1996 Modeling and simulation of crack propagation in mixed-modes interlaminar fracture specimens. *Int. J. Fract.* **77**, 111–140. (doi:10.1007/BF00037233)

35. Xu XP, Needleman A. 1994 Numerical simulations of fast crack growth in brittle solids. *J. Mech. Phys. Solids* **42**, 1397–1434. (doi:10.1016/0022-5096(94)90003-5)

36. Chandra N, Li H, Shet C, Ghonem H. 2002 Some issues in the application of cohesive zone models for metal-ceramic interfaces. *Int. J. Solids Struct.* **39**, 2827–2855. (doi:10.1016/S0020-7683(02)00149-X)

37. Tvergaard V, Hutchinson JW. 1992 The relation between crack growth resistance and fracture process parameters in elastic-plastic solids. *J. Mech. Phys. Solids* **40**, 1377–1397. (doi:10.1016/0022-5096(92)90020-3)

38. Chaboche JL, Girard R, Schaff A. 1997 Numerical analysis of composite systems by using interphase/interface models. *Comput. Mech.* **20**, 3–11. (doi:10.1007/s004660050209)

39. Lin G, Geubelle PH, Sottos NR. 2001 Simulation of fiber debonding with friction in a model composite pushout test. *Int. J. Solids Struct.* **38**, 8547–8562. (doi:10.1016/S0020-7683(01)00085-3)

40. Del Piero G, Raous M. 2010 A unified model for adhesive interfaces with damage, viscosity, and

friction. *Eur. J. Mech. A/Solids* **29**, 496–507. (doi:10.1016/j.euromechsol.2010.02.004)

41.   Alfano G, Sacco E. 2006 Combining interface damage and friction in a cohesive-zone model. *Int. J. Numer. Methods Eng.* **68**, 542–582. (doi:10.1002/nme.1728)

42.   Cocchetti G, Maier G, Shen XP. 2002 Piecewise linear models for interfaces and mixed mode cohesive cracks. *C. - Comput. Model. Eng. Sci.* **3**, 279–298.

43.   Serpieri R, Alfano G. 2011 Bond-slip analysis via a thermodynamically consistent interface model combining interlocking, damage and friction. *Int. J. Numer. Methods Eng.* **85**, 164–186. (doi:10.1002/nme.2961)

44.   Serpieri R, Sacco E, Alfano G. 2015 A thermodynamically consistent derivation of a frictional-damage cohesive-zone model with different mode i and mode II fracture energies. *Eur. J. Mech. A/Solids* **49**, 13–25. (doi:10.1016/j.euromechsol.2014.06.006)

45.   Serpieri R, Alfano G, Sacco E. 2015 A mixed-mode cohesive-zone model accounting for finite dilation and asperity degradation. *Int. J. Solids Struct.* **67–68**, 102–115. (doi:10.1016/j.ijsolstr.2015.04.005)

46.   Serpieri R, Albarella M, Sacco E. 2017 A 3D two-scale multiplane cohesive-zone model for mixed-mode fracture with finite dilation. *Comput. Methods Appl. Mech. Eng.* **313**, 857–888. (doi:10.1016/j.cma.2016.10.021)

47.   ASTM B348-13. 2015 Standard Specification for Titanium and Titanium Alloy Bars and Billets. *Astm.* **02.04**, 8. (doi:10.1520/B0348-13.2)

48.   McDonald DB, Sherman MR, Pfeifer DW, Virmani YP. 1995 Stainless steel reinforcing as corrosion protection. *Concr. Int.* **17**, 65–70.

49.   Higgins C, Knudtsen J, Amneus D, Barker L. 2017 Shear and Flexural Strengthening of Reinforced Concrete Beams with Titanium Alloy Bars. In *Proceedings of the 2nd World Congress on Civil, Structural, and Environmental Engineering (CSEE'17)*, pp. 1–8. (doi:10.11159/icsenm17.141)

50.   Donachie MJ. 2000 Titanium: A Technical Guide, 2nd Edition | Introduction to Selection of Titanium Alloys. *ASM Int.* **180**, 5–11. (doi:10.1361/tatg2000p005)

51.   ISO Standard 6892-1:2016. 2016 Metallic materials - Tensile testing - Part 1: Method of test at room temperature. *Int. Organ. Stand.* , 79. (doi:10.3403/30268532)

52.   RILEM TC. 1983 RC 6 Bond test for reinforcement steel. 2. Pull-out test, 1983. In *RILEM Recommendations for the Testing and Use of Constructions Materials* (ed RILEM), pp. 218–220. E & FN SPON. (doi:10.1617/2351580117.081)

53.   Feenstra PH, de Borst R, Rots JG. 1991 Numerical Study on Crack Dilatancy Part I: Models and Stability Analysis. *J. Eng. Mech.* **117**, 733–753. (doi:https://doi.org/10.1061/(ASCE)0733-9399(1991)117:4(733))

54.   Jorge S, Dias-da-Costa D, Júlio ENBS. 2012 Influence of anti-corrosive coatings on the bond of steel rebars to repair mortars. *Eng. Struct.* **36**, 372–378. (doi:10.1016/j.engstruct.2011.12.028)

55.   Chung L, Jay Kim JH, Yi ST. 2008 Bond strength prediction for reinforced concrete members with highly corroded reinforcing bars. *Cem. Concr. Compos.* **30**, 603–611. (doi:10.1016/j.cemconcomp.2008.03.006)

56.   © ANSYS I. 2018 ANSYS. © *ANSYS, Inc.* , http://www.ansys.com/es_es.

57.   Canonsburg AD. 2015 ANSYS Mechanical User ' s Guide. **15317**, 724–746.